

# Achieving an Order of Magnitude Speed-up in Hybrid Functional and Plane Wave based *Ab Initio* Molecular Dynamics: Applications to Proton Transfer Reactions in Enzymes and in Solution

Sagarmoy Mandal,<sup>1,2</sup> Vaishali Thakkur,<sup>1</sup> and Nisanth N. Nair<sup>1, a)</sup>

<sup>1)</sup>Department of Chemistry, Indian Institute of Technology Kanpur (IITK), Kanpur - 208016, India

<sup>2)</sup>Interdisciplinary Center for Molecular Materials and Computer Chemistry Center, Friedrich-Alexander-Universität Erlangen-Nürnberg (FAU), Nögelsbachstr. 25, 91052 Erlangen, Germany

(Dated: 11 January 2021)

*Ab initio* molecular dynamics (AIMD) with hybrid density functionals and plane wave basis is computationally expensive due to the high computational cost of exact exchange energy evaluation. Recently, we proposed a strategy to combine adaptively compressed exchange (ACE) operator formulation and multiple time step (MTS) integration scheme to reduce the computational cost significantly [*J. Chem. Phys.* **151**, 151102 (2019)]. However, it was found that the construction of the ACE operator, which has to be done at least once in every MD time step, is computationally expensive. In the present work, systematic improvements are introduced to further speed-up by employing localized orbitals for the construction of the ACE operator. By this, we could achieve a computational speed-up of an order of magnitude for a periodic system containing 32-water molecules. Benchmark calculations were carried out to show the accuracy and efficiency of the method in predicting the structural and dynamical properties of bulk water. To demonstrate the applicability, computationally intensive free energy computations at the level of hybrid density functional theory were performed to investigate (a) methyl formate hydrolysis reaction in neutral aqueous medium and (b) proton transfer reaction within the active site residues of class-C  $\beta$ -lactamase enzyme.

## I. INTRODUCTION

*Ab initio* molecular dynamics (AIMD) techniques are extensively used to investigate structural and dynamical properties of a wide variety of molecular systems, and to predict mechanism and free energetics of physiochemical processes.<sup>1-4</sup> In AIMD simulations, interatomic interactions are evaluated on-the-fly using electronic structure calculations at every MD step.<sup>5-8</sup> Kohn Sham density functional theory (KS-DFT) with plane wave (PW) basis set is widely used for performing AIMD simulations of periodic condensed matter systems. The choice of the exchange-correlation (XC) functionals for the KS-DFT calculations determines the accuracy of the predicted properties. Generalized gradient approximation (GGA)<sup>9-11</sup> type XC functionals are most commonly used to carry out AIMD using PW KS-DFT. However, these functionals suffer from self interaction error (SIE)<sup>12-15</sup> where the XC functional erroneously includes the unphysical self-interaction of electron density with itself. Due to the SIE, the XC functionals tend to overdelocalize the electron density, leading to the underestimation of bandgap of solids, reaction barriers, and dissociation energies.<sup>13,15</sup>

SIE can be minimized by using hybrid functionals, where a certain portion of the Hartree-Fock (HF) exchange energy is added to the GGA exchange energy.<sup>12,16-19</sup> Hybrid functionals are generally known to improve the prediction of energetics, structures, electronic properties, chemical reaction barriers and band

gap of solids.<sup>17-29</sup> Also, hybrid functional based AIMD simulations have been shown to improve the description of the structural and dynamical properties of liquids<sup>30-35</sup> as well as the accuracy of the computed free energy surfaces.<sup>36-38</sup> However, AIMD simulation with hybrid functionals and PW basis set is extremely time consuming due to the high computational cost associated with the exact exchange energy evaluation.<sup>39</sup> Thus, it is not a common practice to perform hybrid functional based AIMD simulations for systems containing several hundred or more atoms.

Various possible strategies have been proposed to speed-up such calculations, for example, utilization of localized orbitals,<sup>23,32-34,37,40-48</sup> usage of the multiple time step (MTS) algorithms,<sup>49-51</sup> use of coordinate-scaling approach,<sup>52,53</sup> employment of massively parallel algorithms<sup>54-57</sup> and other approaches.<sup>58,59</sup> Recently, we proposed a robust method<sup>38,60</sup> for performing efficient hybrid functionals and PW based AIMD, where a MTS integrator<sup>1</sup> scheme was employed based on the adaptively compressed exchange (ACE)<sup>61,62</sup> operator formalism. In the proposed method, the ionic forces were artificially partitioned into computationally cheap fast forces and computationally costly slow forces with the help of an approximate representation of the exact exchange operator (i.e. the ACE operator). Using the MTS algorithm, the computationally cheap fast forces were computed more frequently as compared to the computationally costly slow forces, thereby reducing the computational cost of performing such AIMD calculations. Additionally, our method has been shown to be efficient and accurate in predicting the structural and dynamical properties of realistic condensed matter systems.

<sup>a)</sup>Electronic mail: nnair@iitk.ac.in

It was realized that the construction of the ACE operator, which has to be done at least once in every MD time step, is the computational bottleneck. In the present work, we systematically improve the computational speed by employing localized orbitals for the construction of the ACE operator. Specifically, the localized selected column of the density matrix (SCDM)<sup>63</sup> orbitals are used to build the ACE operator. The SCDM method for obtaining localized orbitals is computationally efficient, and the procedure is not iterative (unlike in the case of computing Maximally Localized Wannier Functions). Recently, Carnimeo *et al.*<sup>64</sup> also employed a methodology to speed-up ACE operator construction based on the localized SCDM orbitals. Their implementation in the Quantum ESPRESSO<sup>65</sup> code reported a speed-up of at least 3-4 fold for hybrid functionals and PW based exact exchange energy calculations.

Our approach presented in this paper, termed as s-MTACE, opens up the possibility of performing hybrid DFT based MD simulations of large condensed matter systems providing a speed up of 10 fold or more. After presenting the theory and computational details, benchmark calculations are reported to demonstrate the accuracy and the computational efficiency of the method. In particular, we have investigated the structural and dynamical properties of bulk water for benchmarking purpose. Subsequently, we used our approach to perform free energy calculations of two important proton transfer reactions, namely methyl formate hydrolysis reaction in neutral water employing periodic AIMD simulations (Figure 1), and proton transfer reaction within the active site residues of class-C  $\beta$ -lactamase enzyme complexed with cephalothin drug using quantum-mechanical/molecular-mechanical (QM/MM) simulations (Figure 2). Here we compare the free energies of chemical reactions computed using both PBE (GGA) and PBE0 (hybrid) density functionals. Our results shed light on the performance of the PBE and the PBE0 functionals in predicting free energy barriers of reactions involving proton transfers in solutions and in enzymes from finite temperature MD simulations.

## II. THEORY

KS-DFT calculations with hybrid functionals requires the application of the exact exchange operator  $\mathbf{V}_X = -\sum_j^{N_{\text{orb}}} \frac{|\psi_j\rangle\langle\psi_j|}{r_{12}}$  on each of the KS orbitals  $|\psi_i\rangle$  at each step of the self consistent field (SCF) iterations:

$$\begin{aligned} \mathbf{V}_X|\psi_i\rangle &= -\sum_j^{N_{\text{orb}}} |\psi_j\rangle \langle\psi_j|(r_{12})^{-1}|\psi_i\rangle, \\ &= -\sum_j^{N_{\text{orb}}} v_{ij}(\mathbf{r}_1)|\psi_j\rangle, \quad i = 1, \dots, N_{\text{orb}} \end{aligned} \quad (1)$$

with

$$v_{ij}(\mathbf{r}_1) = \langle\psi_j|(r_{12})^{-1}|\psi_i\rangle. \quad (2)$$

Here,  $N_{\text{orb}}$  is the total number of occupied orbitals. Computation of  $v_{ij}(\mathbf{r})$  is efficiently done in reciprocal

space<sup>39,40</sup> using Fourier transform. If  $N_G$  is the total number of PWs, the computational cost for doing Fourier transform scales as  $N_G \log N_G$  by using the Fast Fourier transform (FFT) algorithm. The total computational overhead scales as  $N_{\text{orb}}^2 N_G \log N_G$ ,<sup>39</sup> as the operation of  $\mathbf{V}_X$  on all the KS orbitals requires  $N_{\text{orb}}^2$  evaluations of  $v_{ij}(\mathbf{r})$ . As a result, such calculations are highly computationally intensive for typical molecular systems of our interest with about 100 atoms.

Whereas, the recently developed ACE operator formulation<sup>61,62</sup> could greatly reduce the computational cost of such calculations. In the ACE operator formulation, the full rank  $\mathbf{V}_X$  operator is approximated by the low rank ACE operator  $\mathbf{V}_X^{\text{ACE}} = -\sum_k^{N_{\text{orb}}} |P_k\rangle\langle P_k|$ . Here,  $\{|P_k\rangle\}$  is the set of ACE projection vectors which can be computed by the decomposition of the  $\mathbf{V}_X$  operator; See Appendix A for more details. Construction of  $\{|P_k\rangle\}$  requires evaluation of  $\{\mathbf{V}_X|\psi_i\rangle\}$ , which is a computationally costly step, because of the  $N_{\text{orb}}^2$  number of evaluations of  $v_{ij}(\mathbf{r})$ .<sup>61</sup> However, once the  $\mathbf{V}_X^{\text{ACE}}$  operator is constructed, the evaluation of the action of this operator on KS orbitals can be done easily with  $N_{\text{orb}}^2$  number of inner products as

$$\mathbf{V}_X^{\text{ACE}}|\psi_i\rangle = -\sum_k^{N_{\text{orb}}} |P_k\rangle \langle P_k|\psi_i\rangle, \quad i = 1, \dots, N_{\text{orb}}. \quad (3)$$

The advantage of the ACE approach is that the cost of applying the  $\mathbf{V}_X^{\text{ACE}}$  operator on each KS orbitals is much less as compared to  $\mathbf{V}_X$  operator.

In our earlier method,<sup>38,60</sup> we took advantage of this particular feature of the ACE operator to combine with the MTS scheme for performing efficient hybrid functional based AIMD. However, the construction of the  $\mathbf{V}_X^{\text{ACE}}$  operator, which has to be done at least once in every MD time step, is computationally demanding. From Equation (2), it is clear that  $v_{ij}(\mathbf{r})$  will be zero for non-overlapping orbital pairs and such pairs of orbitals will not contribute to the sum in Equation (1). Thus, it is possible to speed-up the construction of the ACE operator by employing a screened set of localized orbitals.<sup>64</sup> For systems with finite band gap, a unitary transformation can be carried out to localize the KS orbitals in real space as

$$|\phi_k\rangle = \sum_i^{N_{\text{orb}}} |\psi_i\rangle u_{ik}, \quad (4)$$

where  $u_{ik} \equiv (\mathbf{U})_{ik}$  and  $\mathbf{U}$  is a unitary matrix. Now, by a screening procedure, where least contributing orbitals are neglected, we expect to achieve a substantial decrease in the number of orbitals involved in the evaluation of  $\{\mathbf{V}_X|\psi_i\rangle\}$ .

In our present study, we employed the SCDM method<sup>63</sup> to localize the canonical KS orbitals in real space. In our computations, we employed the following cutoff criteria

$$\int d\mathbf{r} |\phi_i(\mathbf{r})\phi_j^*(\mathbf{r})| \geq \rho_{\text{cut}},$$

to screen the orbital pairs entering in Equation (1). An orbital pair  $i$ - $j$  is only considered during the computation

of the  $\mathbf{V}_X^{\text{ACE}}$  operator if the above criteria is satisfied. The ACE operator computed through the above mentioned screening scheme is denoted as  $\mathbf{V}_X^{\text{s-ACE}}$  (screened ACE operator).

Now, similar to our earlier work,<sup>38,60</sup> we split the individual ionic force components (in hybrid functional based AIMD) for a system containing  $N$  atoms as

$$F_K^{\text{exact}} = F_K^{\text{s-ACE}} + \Delta F_K, \quad K = 1, \dots, 3N \quad (5)$$

with  $\Delta F_K = (F_K^{\text{exact}} - F_K^{\text{s-ACE}})$ . Here,  $\mathbf{F}^{\text{exact}}$  and  $\mathbf{F}^{\text{s-ACE}}$  are the ionic force computed with the full rank exchange operator  $\mathbf{V}_X$  and the low rank  $\mathbf{V}_X^{\text{s-ACE}}$  operator constructed (only) at the beginning of SCF cycles, respectively. As the  $\mathbf{V}_X^{\text{s-ACE}}$  operator closely resembles the  $\mathbf{V}_X$  operator, the differences in the ionic force components of  $\mathbf{F}^{\text{exact}}$  and  $\mathbf{F}^{\text{s-ACE}}$  are very small. Now we make the assumption that  $\mathbf{F}^{\text{s-ACE}}$  is the fast force and  $\Delta \mathbf{F}$  is the slow force. We have verified this assumption during our benchmark calculations. Finally, we employ the reversible reference system propagator algorithm (r-RESPA)<sup>66</sup> to compute the computationally costly  $\Delta \mathbf{F}$  forces less frequently as compared to the cheaper  $\mathbf{F}^{\text{s-ACE}}$  forces, thereby speeding-up the calculations. Specifically,  $\mathbf{F}^{\text{s-ACE}}$  is computed at every small time step  $\delta t$  and  $\Delta \mathbf{F}$  is computed at every  $n$  steps (i.e., with a time step  $\Delta t = n\delta t$ ). Here, the small time step  $\delta t$  can be chosen as per the time scale of fast forces ( $\mathbf{F}^{\text{s-ACE}}$ ) that are cheaper to compute.

### III. COMPUTATIONAL DETAILS

All the calculations presented here were carried out employing a modified version of the CPMD program<sup>67,68</sup> where the proposed s-MTACE method has been implemented. We used PBE0<sup>20</sup> and PBE<sup>11</sup> functionals for all the calculations. The effect of the core electrons were incorporated using the norm-conserving Troullier-Martin type pseudopotentials,<sup>69</sup> generated for PBE functional. For expanding the wavefunctions in PW basis set, a cut-off energy of 80 Ry was used. We carried out Born-Oppenheimer molecular dynamics (BOMD) simulations to perform MD simulations at microcanonical ( $NVE$ ) and canonical ( $NVT$ ) ensembles. Nosé-Hoover chain thermostat<sup>70</sup> was employed to perform canonical ensemble AIMD simulation at 300 K temperature. The wavefunction convergence criteria was set to  $10^{-6}$  a.u. for the orbital gradients during the SCF iterations. For the initial guess of the wavefunctions at every MD step, Always Stable Predictor Corrector Extrapolation scheme<sup>71</sup> of order 5 was used.

#### A. Benchmark Calculations: 32 Water System

We carried out benchmark calculations for bulk water, modelled using 32 water molecules taken in a periodic supercell of dimensions  $9.85 \text{ \AA} \times 9.85 \text{ \AA} \times 9.85 \text{ \AA}$  corresponding to water density  $\sim 1 \text{ g cm}^{-3}$ . Two classes of simulations were performed to benchmark the efficiency and the accuracy of our method:

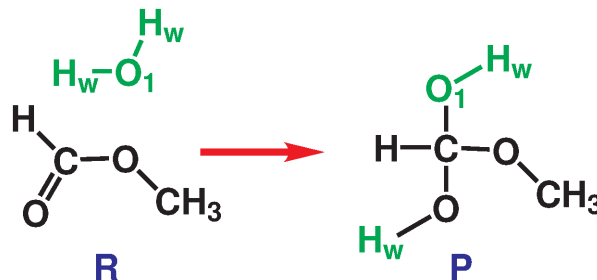


FIG. 1. The formation of the gem-diol intermediate (**P**) from the reactant (**R**) during the methyl formate hydrolysis in neutral aqueous medium. The attacking water molecule is shown in green color.

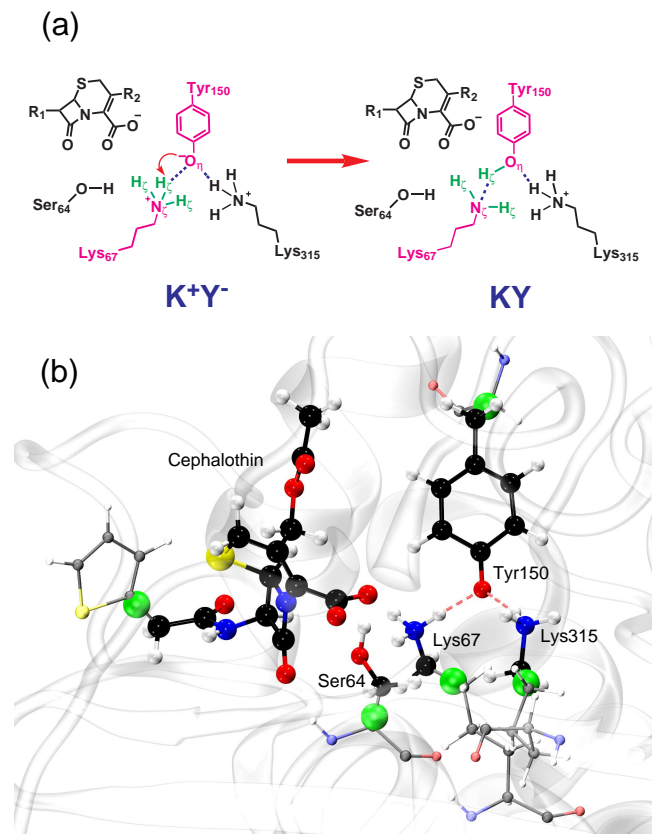


FIG. 2. (a) Proton transfer from protonated Lys<sub>67</sub> to Tyr<sub>150</sub> in presence of cephalothin ( $\mathbf{K}^+\mathbf{Y}^- \rightarrow \mathbf{KY}$ ). The residues involved in the proton transfer are shown in magenta color, and the hydrogen atoms involved are shown in green color. (b) A representative snapshot of the solvated non-covalently complexed drug-substrate (class-C  $\beta$ -lactamase bound to the cephalothin drug molecule) in  $\mathbf{K}^+\mathbf{Y}^-$  state. Active site residues of class-C  $\beta$ -lactamase and the cephalothin drug molecule are shown in CPK style. The atoms shown in glossy spheres were treated by QM. Atom color code: C (black), O (red), N (blue), S (yellow), H (white), and capping H (green).

(a) **VV**: Here, we performed BOMD simulations in  $NVE/NVT$  ensemble with the standard velocity Verlet scheme with a timestep of  $\Delta t$  fs. The value of  $\Delta t$  used for the runs will be specified later in the below sections.

(b) **MTS-n**: Here, we performed BOMD simulations in  $NVE/NVT$  ensemble with s-MTACE scheme with an

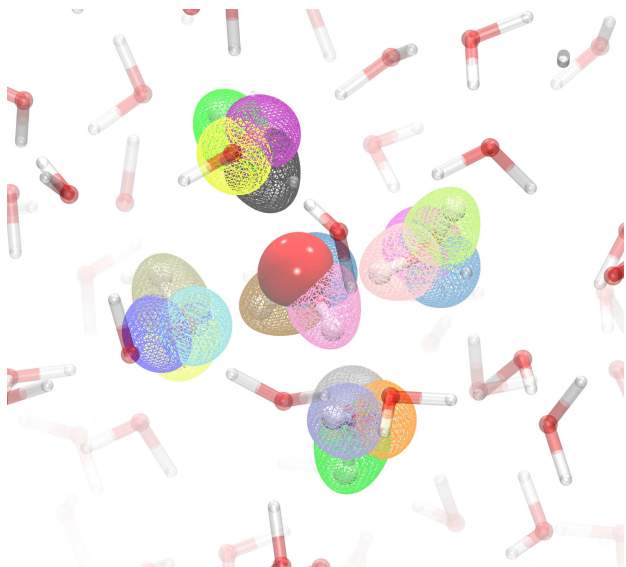


FIG. 3. The SCDM-localized orbitals  $\{\phi_j\}$  (wireframe volumetric representation) considered in the computation of  $v_{ij}$  for a given SCDM-localized orbital  $\phi_i$  (solid-red volumetric representation) while using the cutoff  $\rho_{\text{cut}} = 2.5 \times 10^{-2}$  for a periodic system containing 64 water molecules. Atom color code: Red (O), White (H). Isovalue used for the volumetric representation is  $1 \times 10^{-2}$  a.u.

inner time step,  $\delta t = 0.5$  fs and an outer time step,  $\Delta t = 0.5 \times n$  fs.

Additionally, for these **MTS-n** runs, three different cutoffs ( $\rho_{\text{cut}}$ ) were chosen for constructing  $\mathbf{V}_X^{\text{ACE}}$  operators:  $\rho_{\text{cut}} = 2.0 \times 10^{-3}$ ,  $1.0 \times 10^{-2}$ , and  $2.5 \times 10^{-2}$ . For obtaining a realistic picture, we mention in passing that while using  $\rho_{\text{cut}} = 2.5 \times 10^{-2}$ , Equation 2 is mostly computed over the localized orbitals within the first solvation shell (Figure 3).

## B. Application: Methyl Formate Hydrolysis

A cubic periodic simulation cell with side length of  $10.1 \text{ \AA}$  was chosen for modelling methyl formate hydrolysis in neutral water. The system contained one methyl formate molecule and 32 water molecules. We performed two sets of simulations with the GGA/PBE and hybrid/PBE0 XC functionals. BOMD simulations were carried out to perform MD simulations in canonical ensemble at  $T = 300\text{K}$  temperature employing Nosé-Hoover chain thermostats.<sup>70</sup> For the PBE calculations, the standard velocity Verlet scheme was employed with a timestep of  $\Delta t = 0.48$  fs. Whereas, for the PBE0 runs, s-MTACE with  $\delta t = 0.48$  fs and  $\Delta t = 7.2$  fs (i.e.,  $n = 15$ ) were performed. We used  $\rho_{\text{cut}} = 2.5 \times 10^{-2}$  for the screening of the SCDM orbital pairs.

Well-sliced metadynamics (WS-MTD) approach<sup>72</sup> was employed to compute the free energy surface of the methyl formate hydrolysis reaction. Two collective variables (CVs),  $\mathbf{s} = \{s_1, s_2\}$ , were chosen to explore the free energy surface of the reaction. The distance between the carbonyl carbon atom (C) of the methyl formate and the oxygen atom ( $\text{O}_1$ ) of the attacking water molecule

( $d[\text{C}-\text{O}_1]$ ) is chosen as the first CV ( $s_1$ ), see Figure 1. Sampling along this CV was performed in a controlled manner using the umbrella sampling<sup>73</sup> like bias potential

$$W_h(s_1) = \frac{1}{2} \kappa_h \left( s_1 - d_h^{(0)} \right)^2, \quad h = 1, \dots, M. \quad (6)$$

Here,  $M$  is the total number of umbrella windows used.  $\kappa_h$  and  $d_h^{(0)}$  are the restraining force constant and the equilibrium value of the  $h$ -th umbrella restraint, respectively.

The coordination number ( $CN$ ) of the oxygen atom ( $\text{O}_1$ ) of the attacking water with all the hydrogen atoms ( $\text{H}_w$ ) of the solvent water molecules is chosen as the second CV ( $s_2$ )

$$CN[\text{O}_1 : \text{H}_w] = \sum_{i=1}^{N_{\text{H}_w}} \frac{1}{1 + (d_{1i}/d_0)^6}, \quad (7)$$

with  $d_0 = 1.30 \text{ \AA}$ . Here,  $N_{\text{H}_w}$  is the total number of  $\text{H}_w$  atoms and  $d_{1i}$  is the distance between the  $\text{O}_1$  atom and the  $i$ -th  $\text{H}_w$  atom. This CV was sampled employing the well tempered metadynamics (WT-MTD) bias potential<sup>74</sup>

$$V^b(s_2, t) = \sum_{\tau < t} w(\tau) \exp \left[ -\frac{\{s_2 - s_2(\tau)\}^2}{2(\delta s)^2} \right]. \quad (8)$$

Here,  $\delta s$  is the width of the Gaussian function and the height of the Gaussian,  $w(\tau)$ , is given by,

$$w(\tau) = w_0 \exp \left[ -\frac{V^b(s_2, \tau)}{k_B \Delta T} \right], \quad (9)$$

where  $w_0$  and  $\Delta T$  are parameters and  $k_B$  is the Boltzmann constant.

For each umbrella window  $h$ , we construct the partially reweighted probability distribution

$$P_h(s'_1, s'_2) = \frac{\int_{t_{\text{min}}}^{t_{\text{max}}} dt A_h(t) \prod_{\alpha=1}^2 \delta(s_\alpha(t) - s'_\alpha)}{\int_{t_{\text{min}}}^{t_{\text{max}}} dt A_h(t)} \quad (10)$$

with

$$A_h(t) = \exp [\beta \{V_h^b(s_2(t), t) - c_h(t)\}]$$

and

$$c_h(t) = \frac{1}{\beta} \ln \left[ \frac{\int ds_2 \exp [\beta \theta V^b(s_2, t)]}{\int ds_2 \exp [\beta (\theta - 1) V^b(s_2, t)]} \right].$$

Here,  $\theta = (T + \Delta T) / \Delta T$ , and  $\beta = 1/k_B T$ . The integrals in Equation (10) were evaluated for a time series from  $t_{\text{min}}$  to  $t_{\text{max}}$ . Finally, the weighted histogram analysis method (WHAM)<sup>75</sup> was used to combine the partially reweighted probability distributions  $\{P_h(s_1, s_2)\}$  to get the Boltzmann reweighted probability distribution and free energy.

We have used 36 windows in total for sampling  $d[\text{C}-\text{O}_1]$  in the range from  $1.51$  to  $3.70 \text{ \AA}$ . The parameters of the umbrella sampling bias potential ( $\kappa_h$  and  $d_h^{(0)}$ ) are reported in Appendix B1. The time-dependent bias potential,  $V^b(s_2, t)$ , acting along  $CN[\text{O}_1 : \text{H}_w]$  was updated

every 19.4 fs. The parameters for the WT-MTD bias potential:  $w_0$ ,  $\delta s$  and  $\Delta T$  were chosen to be  $0.59 \text{ kcal mol}^{-1}$ ,  $0.05$ , and  $4000 \text{ K}$ , respectively. Initially, we carried out 2–3 ps of equilibration for each umbrella window. Afterwards, 35 ps of production runs were performed for every window. Additionally, to sample the transition state region more extensively, we generated 46 and 50 ps long trajectories for the windows near the transition state region ( $s_1 \in [1.70, 2.05] \text{ \AA}$ ) for PBE0 and PBE based simulations, respectively.

### C. Application: Protonation State of Active Site Residues of Class-C $\beta$ -Lactamase

The equilibrated initial structure for the solvated non-covalently complexed drug-substrate (class-C  $\beta$ -lactamase bound to the cephalothin drug molecule) was taken from an earlier work by our group;<sup>76</sup> See Figure 2(b). The protein-drug complex was solvated with 13473 TIP3P water molecules in a periodic box of size  $78 \times 77 \times 76 \text{ \AA}^3$ . We used the CPMD/GROMOS interface as available in the CPMD program<sup>67</sup> to carry out the hybrid QM/MM canonical ensemble MD simulations. The protein side chains of Lys<sub>67</sub>, Tyr<sub>150</sub>, Lys<sub>315</sub>, Ser<sub>64</sub>, and the cephalothin molecule (except the thiophene ring) were treated by QM, and the remaining part of the system including the solvent molecules were modelled by MM. Capping hydrogen atoms were used whenever the QM/MM boundary cleaves a chemical bond. In total 66 atoms were taken in a QM box with dimensions  $18 \times 21 \times 22 \text{ \AA}^3$ ; see Figure 2(b) for details. The QM part was treated using KS-DFT and PW. The core electrons of all the QM atoms were accounted using norm-conserving Troullier-Martin type pseudopotentials at the level of PBE and PW cutoff of 70 Ry was taken.<sup>69</sup> MM part was treated using parm99 AMBER<sup>77</sup> force-field. The QM/MM interaction was handled using the electronic coupling scheme developed by Laio *et al.*<sup>78</sup> The QM charge density interacts explicitly with any MM point charge within a range of  $15 \text{ \AA}$ , beyond which the interaction was accounted by considering only the multipole expansion of the charge density up to the quadrupole term. Nearest neighbor lists were updated every 50 steps, and the long-range interaction cutoff of  $20 \text{ \AA}$  was taken. QM/MM BOMD simulations were carried out and the temperature of the system was maintained at 300K using two separate Nosé-Hoover chain thermostats<sup>70</sup> for the QM and MM subsystems.

We performed two sets of simulations: (a) **PBE**: the standard velocity Verlet scheme was employed with a timestep of  $\Delta t = 0.48 \text{ fs}$  and the PBE XC functional was used. (b) **PBE0**: the s-MTACE scheme with  $\delta t = 0.48 \text{ fs}$  and  $\Delta t = 7.2 \text{ fs}$  (i.e.,  $n = 15$ ) were considered and the hybrid PBE0 XC functionals was used. We took  $\rho_{\text{cut}} = 2.0 \times 10^{-3}$  for screening the SCDM-localized orbital pairs.

Umbrella sampling approach<sup>73</sup> was employed to model the proton transfer reaction within the active site residues of class-C  $\beta$ -lactamase enzyme. In particular, we compute here the free energy barrier for the proton transfer between the Lys<sub>67</sub>N $_{\zeta}$  and Tyr<sub>150</sub>O $_{\eta}$  atoms

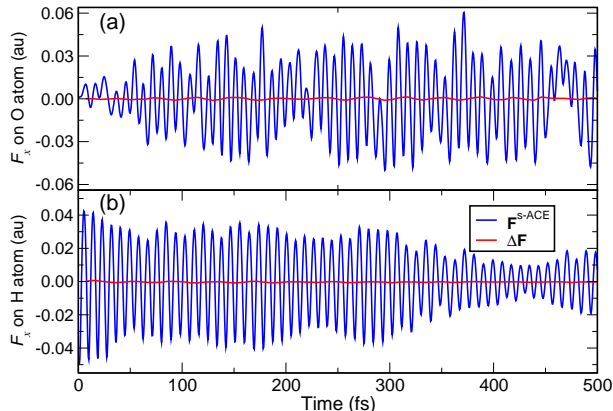


FIG. 4. One of the components of  $\mathbf{F}^{\text{s-ACE}}$  and  $\Delta\mathbf{F}$  on an arbitrarily chosen (a) oxygen and (b) hydrogen atoms for a system containing 32 water molecules in a periodic box during AIMD simulation using PBE0 functional. Screening of the SCDMs-localized orbitals was performed with  $\rho_{\text{cut}} = 2.5 \times 10^{-2}$ .

of class-C  $\beta$ -lactamase in the presence of the substrate; see Figure 2(a). The CN of the Tyr<sub>150</sub>O $_{\eta}$  atom with all the three Lys<sub>67</sub>H $_{\zeta}$  atoms ( $CN[\text{Tyr}_{150}\text{O}_{\eta}:\text{Lys}_{67}\text{H}_{\zeta}]$ ) was biased using the umbrella potential as in Equation (6). The definition of the CN is similar to Equation (7). A total of 24 windows were placed in the range 0.10 to 0.90. Structures with CN lying between 0.0 and 0.5 resemble  $\mathbf{K}^+\mathbf{Y}^-$ , while those between 0.5 and 1.0 are similar to  $\mathbf{KY}$  state; See Figure 2(a). The details of the umbrella bias potentials are reported in Appendix B2. We generated 24 (35) ps long trajectories per each umbrella window during PBE0 (PBE) based QM/MM simulations. The biased probability distributions obtained from these independent simulations were then combined using the WHAM<sup>75</sup> technique to get the Boltzmann reweighted probability distribution, and hence the free energy.

## IV. RESULTS AND DISCUSSION

### A. Benchmark Calculations

To test the accuracy and efficiency of the s-MTACE method, we considered a periodic system containing 32 water molecules modelling bulk water. In Figures 4(a) and (b), we have shown one component of  $\mathbf{F}^{\text{s-ACE}}$  and  $\Delta\mathbf{F}$  (calculated every  $n = \Delta t/\delta t$  steps) on an arbitrarily chosen oxygen and hydrogen atom, respectively. It is apparent that  $\Delta\mathbf{F}$  is slowly varying as compared to  $\mathbf{F}^{\text{s-ACE}}$ . Additionally, the magnitude of  $\Delta\mathbf{F}$  is  $\sim 100$  times smaller as compared to  $\mathbf{F}^{\text{s-ACE}}$ . Thus we conclude that the time scale separation implied in the s-MTACE method is reasonable, as seen in the case of MTACE method.<sup>60</sup>

It is apparent that the efficiency of the MTS schemes crucially depends on the choice of the parameter  $n$ . In practise, one has to determine an optimal value of  $n$  by monitoring the drift in total energy. For this purpose, we compared the total energy fluctuations in velocity Verlet ( $\mathbf{VV}$ ) and MTS runs ( $\mathbf{MTS-n}$ ) with different  $\Delta t$  for 32-water system in  $NVE$  ensemble. To measure the magni-

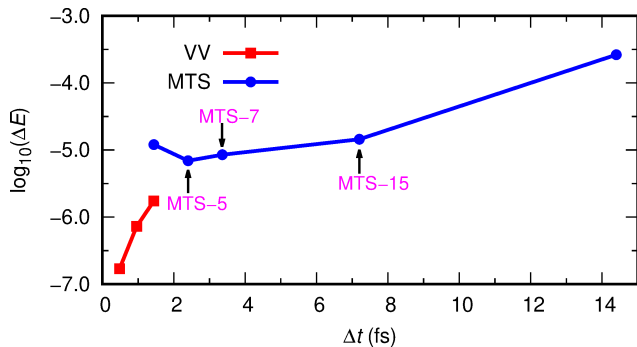


FIG. 5. Measure of the fluctuations in total energy,  $\log_{10}(\Delta E)$ , for different  $\Delta t$  values in **VV** and **MTS- $n$**  simulations using PBE0 functional.  $\Delta E$  is calculated using Equation (11) over 5 ps long trajectories. In these runs, the screening of the SCDM-localized orbitals was performed with  $\rho_{\text{cut}} = 2.5 \times 10^{-2}$ .

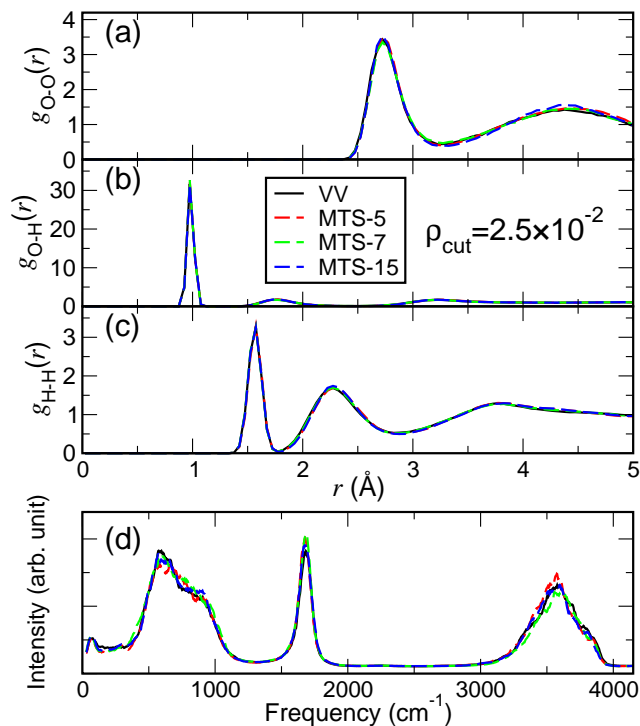


FIG. 6. Radial distribution functions (RDFs) from **VV**, **MTS-5**, **MTS-7** and **MTS-15** simulations of bulk water using PBE0 functional: (a) O-O, (b) O-H, and (c) H-H. (d) Power spectrum of the system computed from these simulations is also presented.

tude of the total energy ( $E$ ) fluctuations, we computed the quantity

$$\Delta E = \left\langle \left| \frac{E - \langle E \rangle}{\langle E \rangle} \right| \right\rangle, \quad (11)$$

for various values of  $n$ . In Figure 5,  $\log_{10}(\Delta E)$  is plotted as a function of the timestep  $\Delta t$  for **VV** and **MTS- $n$**  runs, similar to the analysis done in the earlier works.<sup>50,60</sup> In the case of **VV** runs, it is clear that the total energy fluctuations increase with  $\Delta t$ . For the **MTS- $n$**  runs, the inner timestep  $\delta t$  is kept fixed at  $\sim 0.5$  fs and the outer timestep  $\Delta t = n \delta t$  was varied. In Figure 5, the slope

of the curve is smaller for the **MTS- $n$**  runs as compared to the **VV** runs, indicating that the effect of increasing timestep is less profound in the **MTS** runs. The stability of the **MTS- $n$**  runs with  $n = 15$  (i.e. **MTS-15**) demonstrates that it is a good choice for production runs. Whereas, **MTS- $n$**  simulations with  $n$  greater than 15 were showing substantially high total energy fluctuations and therefore, they were not considered further. Same conclusions about the optimal  $n$  value were obtained while using the different  $\rho_{\text{cut}}$  values (see Appendix C).

To benchmark the accuracy, stability, and efficiency of our proposed method, we performed a few sets of *NVT* simulations with 32-water bulk system. The details of the simulation length, average temperature and drift in total energy for these **VV** and **MTS- $n$**  simulations are reported in Appendix D. The accuracy of the method is benchmarked by comparing the structural and dynamical properties of bulk water obtained from **VV** (which invokes no assumption) and **MTS- $n$**  simulations. In particular, for comparing the structural properties, partial radial distribution functions (RDFs) were computed; See Figure 6(a)-(c). It is clear that the location of the peaks and the peak heights of the RDFs from the **MTS- $n$**  simulations are in excellent agreement with those from the **VV** run. For comparing the dynamical properties, we computed the power spectrum for the same system (shown in Figure 6(d)) by taking the Fourier transform of the velocity auto-correlation function. We have observed that the frequencies and the intensities of the spectra from **VV** and **MTS- $n$**  simulations are in excellent agreement with each other. These results demonstrate that the s-MTACE scheme provides an accurate description of structural and dynamical properties. We have observed a similar trend for different values of  $\rho_{\text{cut}}$ ; See Appendix E.

Now, we study the computational efficiency of our method for which we have compared the average computational time for generating 1 fs trajectory with various parameter settings on an identical computing platform. The CPU time and the achieved speed-ups for various **MTS- $n$**  runs as compared to the **VV** run are reported in Table I for periodic systems with 32, 64 and 128 water molecules. Here, we defined the speed-up for a **MTS- $n$**  run as the ratio between the CPU time per fs in **VV** ( $t_{\text{VV}}$ ) and **MTS- $n$**  runs ( $t_{\text{MTS-}n}$ ):

$$\text{speed-up} = \frac{t_{\text{VV}}}{t_{\text{MTS-}n}}. \quad (12)$$

The time taken per fs in a **MTS- $n$**  run is calculated as:

$$t_{\text{MTS-}n} = \frac{t_{\text{exact}}^{\text{force}} + n t_{\text{s-ACE}}^{\text{force}}}{n} \left( \frac{1 \text{ fs}}{\delta t \text{ fs}} \right). \quad (13)$$

Here,  $t_{\text{exact}}^{\text{force}}$  and  $t_{\text{s-ACE}}^{\text{force}}$  are the times taken for  $\mathbf{F}^{\text{exact}}$  and  $\mathbf{F}^{\text{s-ACE}}$  force calculations, respectively. In every  $n$  MD steps, the force using the exact exchange operator (i.e.  $\mathbf{F}^{\text{exact}}$ ) is calculated only once, and the force using the approximate s-ACE operator (i.e.  $\mathbf{F}^{\text{s-ACE}}$ ) is computed  $n$  times. The total CPU time for the computation of the  $\mathbf{F}^{\text{exact}}$  and  $\mathbf{F}^{\text{s-ACE}}$  forces are decomposed into various contributions in Table II.

From Table II, it is clear that by the screening of orbitals, the computational time required for the construction of the ACE operator has significantly decreased, resulting in a net speed up in the force calculation per MD step; see  $t_{s\text{-ACE}}^{\text{force}}$  in Table II for various values of  $\rho_{\text{cut}}$  and Figure 7. However, we have noticed that the number of SCF cycles required for computing energy/forces ( $N^{\text{SCF}}$ ) increases with screening, due to poor initial guess of wavefunctions. Due to this reason, the overall speed-up in generating 1 fs long trajectory (on average) is not proportional to  $n$  (See Table I). For a 32 water periodic system, we could achieve the maximum speed up (of  $\sim 9\text{X}$ ) using  $\rho_{\text{cut}} = 2.5 \times 10^{-2}$  with MTS-15. The performance was better compared to lower values of  $\rho_{\text{cut}}$  for the same value of  $n$  (Figure 8). As expected, MTS-15 performed better than MTS-7 and MTS-5. Speed-ups of  $\sim 11\text{X}$  and  $\sim 13\text{X}$  were observed for 64 and 128 water molecules systems, respectively.

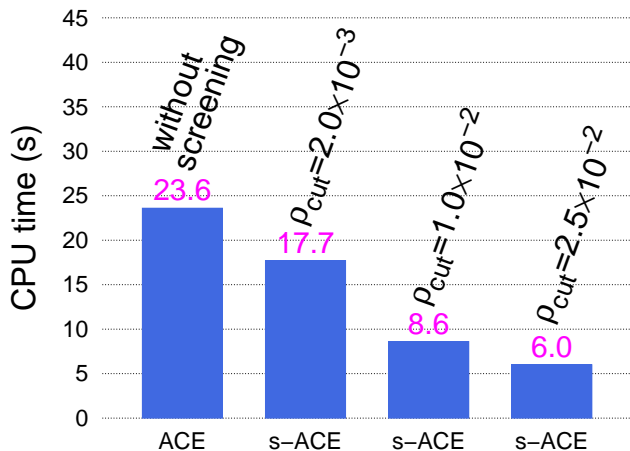


FIG. 7. Average computing time for the construction of  $\mathbf{V}_X^{\text{s-ACE}}$  for various values of  $\rho_{\text{cut}}$  for a periodic system containing 32 water molecules and using 120 identical processors; see also Table II.

## B. Application: Methyl Formate Hydrolysis

The hydrolysis of carboxylic esters is one of the well studied reaction in the field of chemistry, biochemistry and industrial chemistry. Methyl formate hydrolysis serves as the simplest model for the hydrolysis of carboxylic esters and has been well studied experimentally<sup>80–84</sup> and theoretically.<sup>85–89</sup> In our present work, we modelled the methyl formate hydrolysis reaction in neutral water. This reaction happens through proton transfer between solvent and the solute. Neutral hydrolysis of methyl formate leads to the formation of formic acid and methanol. It follows a stepwise mechanism, where addition of a solvent water molecule to the carbonyl group results in a stable gem-diol intermediate (see Figure 1), followed by the decomposition of the intermediate to the final products.<sup>88,89</sup> In our work, we focus only on the elementary step leading to the formation of the gem-diol intermediate. The free energetics

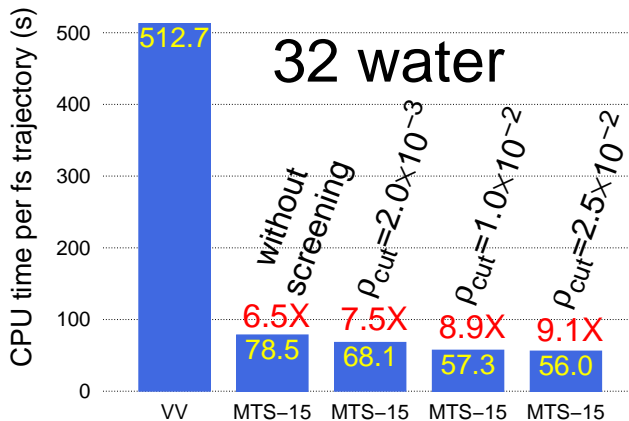


FIG. 8. Average computational time for generating 1 fs trajectory with PBE0 for a system containing 32 water molecules in a periodic box using the exact  $\mathbf{V}_X$  operator (VV), and s-MTACE with  $n = 15$  (MTS-15) for various values of  $\rho_{\text{cut}}$ . All the computations were performed using identical 120 processors. The computational time reported here is averaged over 630 MD steps.

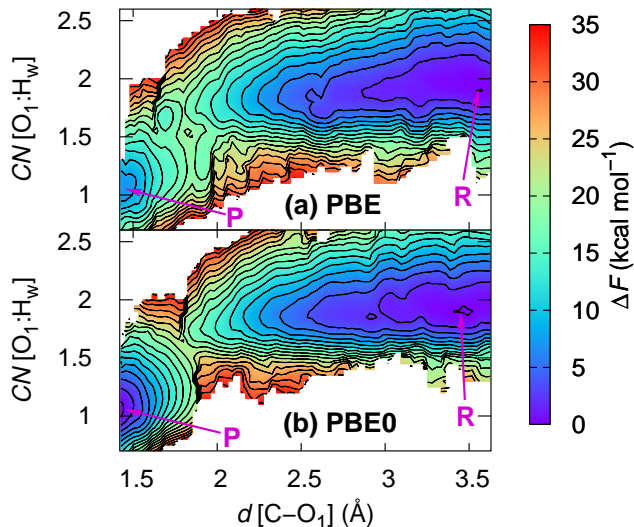


FIG. 9. Free energy surfaces computed using (a) PBE and (b) PBE0 density functionals for the  $\mathbf{R} \rightarrow \mathbf{P}$  reaction are presented. Contour lines are drawn every  $2 \text{ kcal mol}^{-1}$ .

for this reaction step were computed using the WS-MTD technique.

For reweighting the WT-MTD bias potential, we used  $t_{\text{min}} = 20 \text{ ps}$  and  $t_{\text{max}} = 35 \text{ ps}$ . For the umbrella windows near the transition state region, we took  $t_{\text{max}}$  as 46 (50) ps for the PBE0 (PBE) simulations to obtain better statistics. Here,  $t_{\text{min}}$  was chosen such that the free energy estimate is independent of the initial configuration. The time series plots of the CVs for some of these umbrella windows are shown in Appendix F. The reconstructed free energy surfaces are shown in Figure 9. The convergence of free energy barriers as a function of

TABLE I. Average computational time for generating 1 fs trajectory ( $t_{\text{CPU}}$ ) for periodic systems containing 32, 64 and 128 water molecules using PBE0. The averages were calculated over  $N_{\text{MD}}$  number of MD steps. The achieved speed-ups for various **MTS-n** runs are compared with the **VV** run.<sup>79</sup>

System size	No. of CPU cores	Method	$N_{\text{MD}}$	$\rho_{\text{cut}} = 2.0 \times 10^{-3}$		$\rho_{\text{cut}} = 1.0 \times 10^{-2}$		$\rho_{\text{cut}} = 2.5 \times 10^{-2}$	
				$t_{\text{CPU}}$ (s)	speed-up	$t_{\text{CPU}}$ (s)	speed-up	$t_{\text{CPU}}$ (s)	speed-up
32 water	120	<b>VV</b>	630	518	1.0	509	1.0	512	1.0
		<b>MTS-5</b>	630	127	4.1	129	4.0	136	3.8
		<b>MTS-7</b>	630	103	5.0	98	5.2	101	5.1
		<b>MTS-15</b>	630	70	7.4	57	8.9	56	9.2
64 water	160	<b>VV</b>	105	3962	1.0	3969	1.0	3976	1.0
		<b>MTS-5</b>	105	856	4.6	936	4.2	1059	3.8
		<b>MTS-7</b>	105	656	6.0	692	5.7	792	5.0
		<b>MTS-15</b>	105	396	10.0	371	10.7	402	9.9
128 water	200	<b>VV</b>	5	32668	1.0	32783	1.0	32726	1.0
		<b>MTS-5</b>	15	6400	5.1	7607	4.3	8525	3.8
		<b>MTS-7</b>	21	4914	6.6	5562	5.9	6020	5.4
		<b>MTS-15</b>	45	2611	12.5	2749	11.9	2998	10.9

TABLE II. The decomposition of the total computing time for force calculations for a periodic system containing 32 water molecules. Timings are in seconds when using identical 120 CPU cores. Here,  $t_{\text{s-ACE}}^{\text{Con}}$  is the computing time for the construction of  $\mathbf{V}_X^{\text{s-ACE}}$ ,  $t_{\text{s-ACE}}$  is the computing time per SCF cycle using  $\mathbf{V}_X^{\text{s-ACE}}$ ,  $N_{\text{s-ACE}}^{\text{SCF}}$  is the average number of SCF cycles during the computation of  $\mathbf{F}^{\text{s-ACE}}$ ,  $t_{\text{s-ACE}}^{\text{force}}$  is the total computing time for the calculation of  $\mathbf{F}^{\text{s-ACE}}$ ,  $t_{\text{exact}}$  is the computing time per SCF cycle using  $\mathbf{V}_X$ ,  $N_{\text{exact}}^{\text{SCF}}$  is the average number of SCF cycles for  $\mathbf{F}^{\text{exact}}$  force calculation,  $t_{\text{exact}}^{\text{force}}$  is the total computing time for the calculation of  $\mathbf{F}^{\text{exact}}$ ,  $t_{\text{s-ACE}}^{\text{force}} = t_{\text{s-ACE}}^{\text{Con}} + N_{\text{s-ACE}}^{\text{SCF}} t_{\text{s-ACE}}$ , and  $t_{\text{exact}}^{\text{force}} = N_{\text{exact}}^{\text{SCF}} t_{\text{exact}}$ .

Method	$\rho_{\text{cut}}$	$t_{\text{s-ACE}}^{\text{Con}}$	$t_{\text{s-ACE}}$	$N_{\text{s-ACE}}^{\text{SCF}}$	$t_{\text{s-ACE}}^{\text{force}}$	$t_{\text{exact}}$	$N_{\text{exact}}^{\text{SCF}}$	$t_{\text{exact}}^{\text{force}}$
<b>VV</b>	–	–	–	–	–	23.6	10.4	245.4
<b>MTS-15</b>	without screening	23.6	0.15	10.1	25.1	23.6	8.0	188.8
<b>MTS-15</b>	$2.0 \times 10^{-3}$	17.7	0.15	10.9	19.3	23.6	8.6	203.0
<b>MTS-15</b>	$1.0 \times 10^{-2}$	8.6	0.15	12.6	10.5	23.6	11.0	259.6
<b>MTS-15</b>	$2.5 \times 10^{-2}$	6.0	0.15	13.4	8.0	23.6	12.0	283.2

TABLE III. Free energy barriers ( $\Delta F^\ddagger$ ) of the reaction  $\mathbf{R} \rightarrow \mathbf{P}$  (Figure 1) using PBE and PBE0 functionals are compared with the experimental estimate.

Method	$\Delta F^\ddagger$ (kcal mol <sup>-1</sup> )
PBE	18.4
PBE0	20.8
Experiment <sup>80</sup>	28.8

$t_{\text{max}}$  is reported in Appendix G1. The converged free energy barriers and the experimental estimate are listed in Table III.

From the free energy surfaces computed using both PBE and PBE0, it can be seen that the locations of the minimum corresponding to the reactant state  $\mathbf{R}$  and the intermediate  $\mathbf{P}$  are nearly the same. However, the topology of the free energy surfaces near the transition state region has some difference. Additionally, the free energy barriers differ between the two functionals. The converged free energy barrier computed using PBE is 18.4 kcal/mol, while that using PBE0 is 20.8 kcal mol<sup>-1</sup>.

The PBE0 free energy barrier is about 2.4 kcal mol<sup>-1</sup> higher than that of PBE, in line with the trends seen for the hydrolysis of formamide in water.<sup>37,38</sup> Notably, the free energy barrier computed from PBE0 is closer to the experimentally “estimated” free energy barrier of 28.8 kcal mol<sup>-1</sup> at 298 K<sup>80</sup> for the reaction under neutral condition. For simple amides, the free energy barrier for neutral hydrolysis was reported to be between 21.9 to 23.8 kcal mol<sup>-1</sup>.<sup>90</sup>

The PBE0 estimate of free energy barrier deviates substantially ( $\sim 8$  kcal mol<sup>-1</sup>) from the experimental data. This may be due to several reasons. It is likely that under neutral aqueous conditions, the rate determining step is the subsequent elimination and not the formation of the gem-diol,<sup>91</sup> different to what is observed under acidic condition.<sup>81</sup> Finite size effects can also affect the results, especially since the transition state configurations have an additional proton dissolved in water. Clearly, a more detailed investigation is warranted in this direction to understand the deviation from the experimental data. Nonetheless, the observed effect of hybrid functional on the free energy barrier is the most significant result of this study. We also note in passing that



the previous computational studies have reported a range of free energy barriers for this reaction at 298 K. Guaydin *et al.*<sup>88</sup> reported that autoionization of water is the rate-determining step and the free energy barrier was predicted to be 23.8 kcal mol<sup>-1</sup> (which in turn was taken from experiment data). Arroyo *et al.*<sup>89</sup> reported a free energy barrier of 28.17 kcal mol<sup>-1</sup> based on their MD simulations using empirical potentials.

### C. Application: Proton Transfer Reactions within the Active Site Residues of Class-C $\beta$ -Lactamase

$\beta$ -Lactam antibiotics are commonly prescribed against bacterial infections. They inhibit the bacterial cell-wall synthesizing enzymes known as penicillin binding proteins (PBPs).<sup>92,93</sup> However, the clinical efficacy of these life saving drugs is progressively deteriorating due to the emergence of drug-resistance in bacteria, primarily associated with the expression of  $\beta$ -lactamases.<sup>93-95</sup> These enzymes hydrolyze  $\beta$ -lactam antibiotics in an efficient manner, preventing the drug molecules to react with PBPs. In the past, our group has contributed to the understanding of the mechanism of hydrolysis of different classes of  $\beta$ -lactamases.<sup>76,96-100</sup> Here, we focus on class-C serine  $\beta$ -lactamases that is majorly responsible for hospital acquired infections. It was found that the protonation states of the active site residues Lys<sub>67</sub> and Tyr<sub>150</sub> of class-C  $\beta$ -lactamase play a crucial role in determining the hydrolysis mechanism.<sup>76,96,97</sup> In the Michaelis complex of cephalothin and the enzyme, two protonation states are possible:  $\mathbf{K}^+\mathbf{Y}^-$  and  $\mathbf{KY}$ . In  $\mathbf{K}^+\mathbf{Y}^-$ , Lys<sub>67</sub> is in the protonated form, while Tyr<sub>150</sub> is in its deprotonated form. On the other hand, both Lys<sub>67</sub> and Tyr<sub>150</sub> are in their neutral forms in the  $\mathbf{KY}$  state (Figure 2(a)). Depending on the protonation state, the general base that activates Ser<sub>64</sub> could differ, rendering different acylation mechanisms.

In the previous study,<sup>76</sup> the free energy barrier for the proton transfer between Lys<sub>67</sub> and Tyr<sub>150</sub> ( $\mathbf{K}^+\mathbf{Y}^- \rightarrow \mathbf{KY}$ ) was found to be small ( $\sim 1$  kcal/mol) at the level of PBE. It was found that, Lys<sub>67</sub> is hydrogen bonded to Ser<sub>64</sub> in the  $\mathbf{KY}$  state and the former residue acts as the general base. Here, we revisited the same problem and computed the free energy barrier separating the  $\mathbf{KY}$  and  $\mathbf{K}^+\mathbf{Y}^-$  states. It is known that PBE can underestimate the proton transfer barriers, and thus studying the above problem using a higher level of theory, especially including the contributions of HF exchange, is crucial.<sup>29</sup> We computed free energies using QM/MM MD with PBE and PBE0 density functionals, and compared their performance.

Umbrella sampling simulations were carried out and the reconstructed free energy surface along the coordinate  $CN[\text{Tyr}_{150}\text{O}_\eta : \text{Lys}_{67}\text{H}_\zeta]$  using the two density functionals are shown in Figure 10. The convergence of the free energy barriers as a function of simulation length is reported in Appendix G2. Also, the error in the computed free energy was calculated using the method given by Hummer *et al.*<sup>101</sup> For both the functionals, the location of the reactant minima ( $\mathbf{K}^+\mathbf{Y}^-$ ) is around  $CN \in [0.3, 0.4]$  (unitless). Whereas, the product minima

( $\mathbf{KY}$ ) is located near  $CN \in [0.8, 0.9]$  (unitless). However, we can notice qualitative and quantitative differences in free energy profiles. At the level of PBE, the free energy barrier for the proton transfer in forward direction ( $\mathbf{K}^+\mathbf{Y}^- \rightarrow \mathbf{KY}$ ) is 1.7 kcal mol<sup>-1</sup>, and the barrier for the proton transfer in the reverse direction ( $\mathbf{KY} \rightarrow \mathbf{K}^+\mathbf{Y}^-$ ) is 0.9 kcal mol<sup>-1</sup>. On the other hand, at the PBE0 level, the barrier for the forward proton transfer is 1.2 kcal mol<sup>-1</sup>, and the barrier for the reverse proton transfer is 2.0 kcal mol<sup>-1</sup>. The error in the free energy estimates is less than 0.3 kcal mol<sup>-1</sup>. Notably,  $\mathbf{K}^+\mathbf{Y}^-$  is predicted to be the most stable state with PBE whereas,  $\mathbf{KY}$  is the most stable state with PBE0. In the earlier study<sup>76</sup> using PBE and QM/MM metadynamics simulation, it was reported that both of the states are equally stable with only  $\sim 1$  kcal mol<sup>-1</sup> barrier for their inter conversion (in the presence of the substrate). This is consistent with the results of the present work using PBE. Although, at the PBE0 level, the most stable state is found to be different, the free energy difference between the two protonation states and the free energy barriers for proton transfer reactions are small. This implies that quick proton transfer between the Tyr<sub>150</sub> and Lys<sub>67</sub> residues can take place at ambient temperature. Therefore we conclude that class-C  $\beta$ -lactamase catalyzed acylation mechanism of the hydrolysis of cephalothin, wherein the deprotonated form of Lys<sub>67</sub> activates Ser<sub>64</sub>,<sup>97</sup> is justified at the PBE0 level.

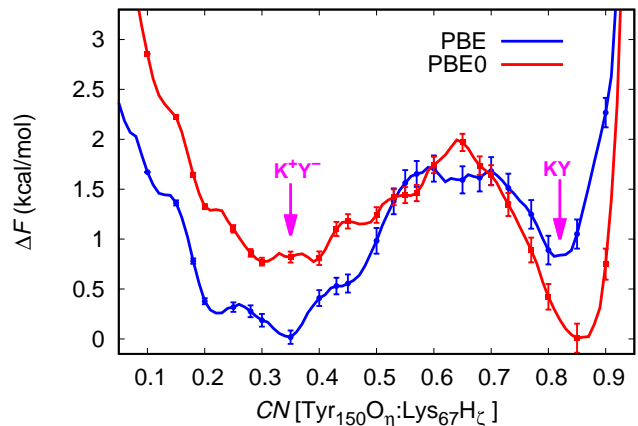


FIG. 10. Free energy as a function of  $CN[\text{Tyr}_{150}\text{O}_\eta : \text{Lys}_{67}\text{H}_\zeta]$  coordinate computed for the proton transfer reaction ( $\mathbf{K}^+\mathbf{Y}^- \rightleftharpoons \mathbf{KY}$ ) using umbrella sampling simulations at the level of PBE (blue) and PBE0 (red) density functionals. Errors in the free energy estimates were computed following Ref. 101.

## V. CONCLUSIONS

In summary, we presented a new scheme named s-MTACE to perform efficient hybrid functional based AIMD simulations using PW basis set. In particular, we have shown that screening the localized orbitals and computing ACE operator using the screened orbitals is an

efficient way to speed up our earlier method.<sup>38,60</sup> Benchmark results show that dynamic and structural properties can be computed accurately using the s-MTACE method. We achieved a computational speed-up of  $\approx 10$  for a periodic 32-water molecules system compared to the conventional implementation of the hybrid functional PW-DFT. For a larger system with 128 water molecules, we have achieved a speed-up of about 13.

Using our implementation, we show that it is possible to carry out computationally demanding free energy calculations at the level of hybrid density functionals. We demonstrated this by performing free energy calculations in two systems involving proton transfer reactions. First, our implementation was combined with the WS-MTD method to study the methyl formate hydrolysis in neutral aqueous solution. The two dimensional free energy surface for this reaction was computed with PBE and PBE0 functionals. We observed that the free energy barrier computed using PBE is 2.4 kcal/mol lower than PBE0, similar to our observations in earlier studies for a different system.<sup>37,38</sup> By employing our method within the framework of QM/MM, we investigated the proton transfer reaction between the active site residues in the Michaelis complex of class-C  $\beta$ -lactamase and cephalothin antibiotic. We found that the stability of protonation states and the free energy barriers for proton transfer are altered while switching from PBE to PBE0.

The general observation of underestimation of proton transfer barriers by PBE compared to PBE0 is consistent with the detailed benchmarking studies by Adamo and co-workers<sup>29</sup> through structural optimizations of several gas-phase reactions. As this work enables us to perform free energy calculations at the level of hybrid functionals within AIMD simulations in an efficient manner, we hope that the presented method and the results obtained from our calculations are of great importance to scientists working in the area of computational catalysis.

## ACKNOWLEDGMENTS

The authors thank Tobias Klöffel and Bernd Meyer for helpful discussions. Financial support from the Science and Engineering Research Board (India) under the MATRICS scheme (Ref. No. MTR/2019/000359) and from the German Research Foundation (DFG) through Research Unit FOR 1878 (funCOS) and Collaborative Research Center SFB 953 (project number 182849149) is gratefully acknowledged. SM and VT thank the University Grant Commission (UGC), India, and IITK for their Ph.D. fellowships. Computational resources were provided by the HPC facility (HPC2013) at IITK, the Erlangen Regional Computing Center (RRZE) at FAU and SuperMUC-NG (project pn98fa) at Leibniz Supercomputing Centre (LRZ).

## Appendix A: Construction of the Adaptively Compressed Exchange Operator

According to the ACE operator formalism, the ACE operator ( $\mathbf{V}_X^{\text{ACE}}$ ) can be constructed through the following series of simple linear algebra operations. First, the exact exchange operator ( $\mathbf{V}_X$ ) has to be applied on the set of KS orbitals  $\{|\psi_i\rangle\}$  as

$$|W_i\rangle = \mathbf{V}_X|\psi_i\rangle, \quad i = 1, \dots, N_{\text{orb}} . \quad (\text{A1})$$

Now, ACE formalism defines  $\mathbf{V}_X^{\text{ACE}}$  as

$$\mathbf{V}_X^{\text{ACE}} = \sum_{i,j}^{N_{\text{orb}}} |W_i\rangle B_{ij} \langle W_j| . \quad (\text{A2})$$

Here,  $\mathbf{B} = \mathbf{M}^{-1}$ , and the matrix  $\mathbf{M}$  has elements

$$M_{kl} = \langle \psi_k | \mathbf{V}_X | \psi_l \rangle . \quad (\text{A3})$$

Now, the Cholesky factorization of  $-\mathbf{M}$  gives

$$\mathbf{M} = -\mathbf{L}\mathbf{L}^T , \quad (\text{A4})$$

where,  $\mathbf{L}$  is a lower triangular matrix. Then  $\mathbf{B}$  is computed as

$$\mathbf{B} = -\mathbf{L}^{-T}\mathbf{L}^{-1} . \quad (\text{A5})$$

Finally, the  $\mathbf{V}_X^{\text{ACE}}$  operator can be rewritten as

$$\mathbf{V}_X^{\text{ACE}} = - \sum_k^{N_{\text{orb}}} |P_k\rangle \langle P_k| , \quad (\text{A6})$$

with  $\{|P_k\rangle\}$  as the columns of the matrix  $\mathbf{P}$ , which is defined as

$$\mathbf{P} = \mathbf{W}\mathbf{L}^{-T} . \quad (\text{A7})$$

## Appendix B: Details of the Umbrella Sampling Bias Parameters

### 1. Methyl Formate Hydrolysis

TABLE B.1. Umbrella sampling parameters: Here,  $d_h^{(0)}$  is in Å and  $\kappa_h$  is in Hartree Bohr<sup>-2</sup>.

$h$	$d_h^{(0)}$	$\kappa_h$	$h$	$d_h^{(0)}$	$\kappa_h$
1	1.51	0.4	19	2.21	0.4
2	1.60	0.2	20	2.25	0.4
3	1.63	0.4	21	2.30	0.2
4	1.65	0.8	22	2.39	0.4
5	1.67	0.8	23	2.43	0.4
6	1.70	0.8	24	2.50	0.2
7	1.73	0.8	25	2.60	0.2
8	1.76	0.8	26	2.70	0.2
9	1.81	0.8	27	2.80	0.2
10	1.83	0.8	28	2.90	0.2
11	1.86	0.8	29	3.00	0.2
12	1.90	0.8	30	3.10	0.2
13	1.93	0.8	31	3.20	0.2
14	1.96	0.8	32	3.30	0.2
15	1.99	0.4	33	3.40	0.2
16	2.05	0.4	34	3.50	0.2
17	2.12	0.4	35	3.60	0.2
18	2.17	0.4	36	3.70	0.2

### 2. Protonation State of Active Site Residues of Class-C $\beta$ -Lactamase

TABLE B.2. Umbrella sampling parameters: Here,  $d_h^{(0)}$  is unitless and  $\kappa_h$  is in Hartree.

$h$	$d_h^{(0)}$	$\kappa_h$	$h$	$d_h^{(0)}$	$\kappa_h$
1	0.10	2.0	13	0.53	1.2
2	0.15	1.5	14	0.55	1.2
3	0.18	2.0	15	0.57	1.5
4	0.20	1.5	16	0.60	1.5
5	0.25	1.5	17	0.65	1.5
6	0.28	1.5	18	0.68	1.5
7	0.30	1.5	19	0.70	1.2
8	0.35	1.5	20	0.73	1.2
9	0.40	1.5	21	0.77	1.2
10	0.43	1.5	22	0.80	1.2
11	0.45	1.5	23	0.85	1.2
12	0.50	1.5	24	0.90	1.2

## Appendix C: Comparison of the Drift in Total Energy for VV and MTS Simulations in the NVE Ensemble

TABLE C.1. The drift in total energy and  $\log_{10}(\Delta E)$  for various **VV** and **MTS-n** simulations in *NVE* ensemble. The results of **MTS-n** simulations with various  $\rho_{\text{cut}}$  values are reported.

Method	$\rho_{\text{cut}}$	Timestep (fs)	Drift <sup>a</sup> (au/ps/atom)	$\log_{10}(\Delta E)$
<b>VV</b>	–	0.48	$1.8 \times 10^{-7}$	-6.77
<b>VV</b>	–	0.96	$1.6 \times 10^{-6}$	-6.14
<b>VV</b>	–	1.44	$2.7 \times 10^{-6}$	-5.76
<b>MTS-3</b>	$2.0 \times 10^{-3}$	1.44	$2.4 \times 10^{-5}$	-5.01
<b>MTS-5</b>	$2.0 \times 10^{-3}$	2.40	$8.7 \times 10^{-6}$	-5.41
<b>MTS-7</b>	$2.0 \times 10^{-3}$	3.36	$5.9 \times 10^{-6}$	-5.54
<b>MTS-15</b>	$2.0 \times 10^{-3}$	7.20	$8.2 \times 10^{-6}$	-5.45
<b>MTS-30</b>	$2.0 \times 10^{-3}$	14.40	$3.1 \times 10^{-4}$	-3.79
<b>MTS-3</b>	$1.0 \times 10^{-2}$	1.44	$2.4 \times 10^{-5}$	-5.00
<b>MTS-5</b>	$1.0 \times 10^{-2}$	2.40	$5.1 \times 10^{-6}$	-5.47
<b>MTS-7</b>	$1.0 \times 10^{-2}$	3.36	$2.0 \times 10^{-5}$	-5.11
<b>MTS-15</b>	$1.0 \times 10^{-2}$	7.20	$1.2 \times 10^{-5}$	-5.32
<b>MTS-30</b>	$1.0 \times 10^{-2}$	14.40	$4.3 \times 10^{-4}$	-3.65
<b>MTS-3</b>	$2.5 \times 10^{-2}$	1.44	$2.3 \times 10^{-5}$	-4.92
<b>MTS-5</b>	$2.5 \times 10^{-2}$	2.40	$4.1 \times 10^{-6}$	-5.16
<b>MTS-7</b>	$2.5 \times 10^{-2}$	3.36	$2.2 \times 10^{-5}$	-5.07
<b>MTS-15</b>	$2.5 \times 10^{-2}$	7.20	$4.1 \times 10^{-5}$	-4.84
<b>MTS-30</b>	$2.5 \times 10^{-2}$	14.40	$4.8 \times 10^{-4}$	-3.58

<sup>a</sup> Drift was calculated as  $|\langle E(t) - E(0) \rangle|/\text{number of atoms/time}$ . Here,  $E(t)$  is the total energy at any time  $t$ .

## Appendix D: Accuracy of VV and MTS Simulations in the NVT Ensemble

TABLE D.1. The simulation time length, average temperature ( $\langle T \rangle$ ) and drift in total energy for various **VV** and **MTS-n** (for various values of  $\rho_{\text{cut}}$ ) runs in *NVT* ensemble.

Method	$\rho_{\text{cut}}$	Timestep (fs)	Length (ps)	$\langle T \rangle$ (K)	Drift <sup>a</sup> (au/ps/atom)
<b>VV</b>	–	0.48	10	301	$1.8 \times 10^{-6}$
<b>MTS-5</b>	$2.0 \times 10^{-3}$	2.40	10	299	$7.8 \times 10^{-6}$
<b>MTS-7</b>	$2.0 \times 10^{-3}$	3.36	10	299	$1.0 \times 10^{-5}$
<b>MTS-15</b>	$2.0 \times 10^{-3}$	7.20	10	300	$6.6 \times 10^{-6}$
<b>MTS-5</b>	$1.0 \times 10^{-2}$	2.40	10	300	$7.6 \times 10^{-6}$
<b>MTS-7</b>	$1.0 \times 10^{-2}$	3.36	10	300	$1.5 \times 10^{-5}$
<b>MTS-15</b>	$1.0 \times 10^{-2}$	7.20	10	300	$8.0 \times 10^{-6}$
<b>MTS-5</b>	$2.5 \times 10^{-2}$	2.40	10	299	$4.3 \times 10^{-6}$
<b>MTS-7</b>	$2.5 \times 10^{-2}$	3.36	10	299	$1.7 \times 10^{-5}$
<b>MTS-15</b>	$2.5 \times 10^{-2}$	7.20	10	300	$2.5 \times 10^{-5}$

<sup>a</sup> Drift was calculated as  $|\langle E(t) - E(0) \rangle|/\text{number of atoms/time}$ . Here,  $E(t)$  is the total energy at any time  $t$ .

### Appendix E: Comparison of Structural and Dynamical Properties

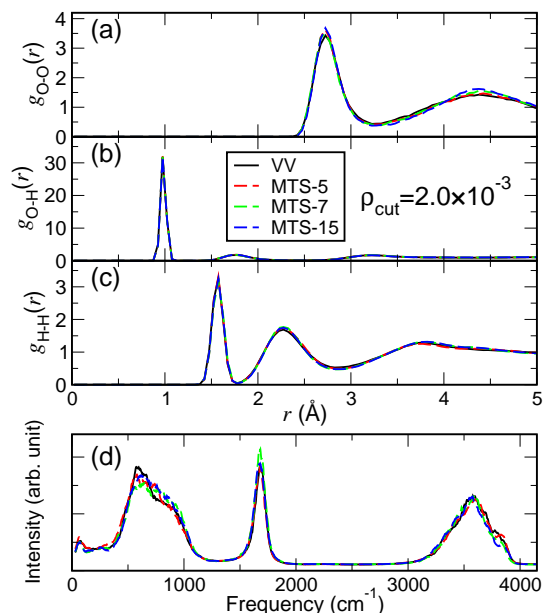


FIG. E.1. Radial distribution functions (RDFs) for bulk water (32 water system) simulation using **VV**, **MTS-5**, **MTS-7** and **MTS-15** trajectories at the level of PBE0: (a) O-O, (b) O-H, and (c) H-H. (d) Power spectrum of the same system computed from **VV**, **MTS-5**, **MTS-7** and **MTS-15** trajectories are shown. Screening of the SCDMs was performed with  $\rho_{\text{cut}} = 2.0 \times 10^{-3}$ .

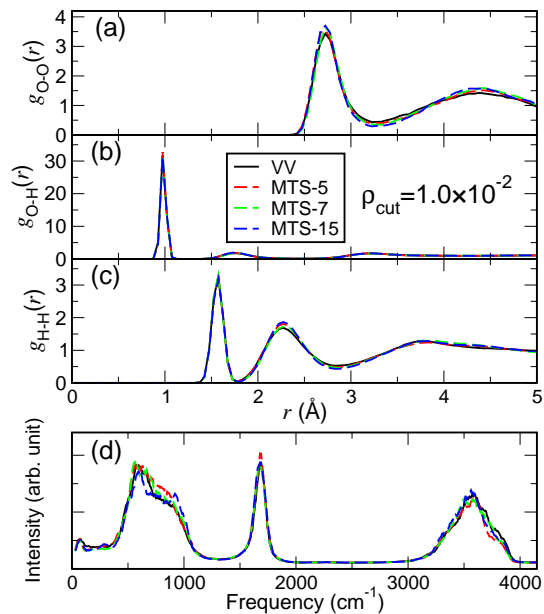


FIG. E.2. Radial distribution functions (RDFs) for bulk water (32 water system) simulation using **VV**, **MTS-5**, **MTS-7** and **MTS-15** trajectories at the level of PBE0: (a) O-O, (b) O-H, and (c) H-H. (d) Power spectrum of the same system computed from **VV**, **MTS-5**, **MTS-7** and **MTS-15** trajectories are shown. Screening of the SCDMs was performed with  $\rho_{\text{cut}} = 1.0 \times 10^{-2}$ .

### Appendix F: Time Series Plots of the CVs for Umbrella Windows Near the Transition State Region

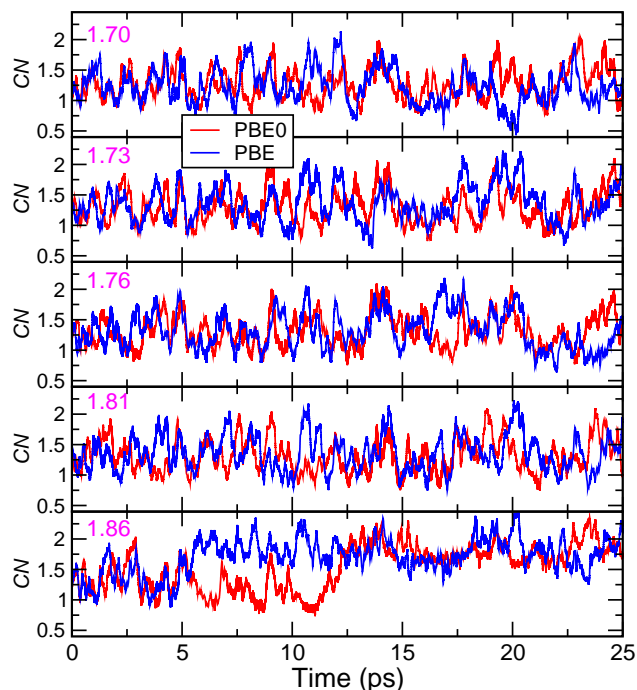


FIG. F.1. Fluctuations in the  $\text{CN}[\text{O}_1 : \text{H}_w]$  CV with simulation time for the umbrella windows near the transition state region (from 1.70 to 1.86 Å) using PBE and PBE0 functionals.

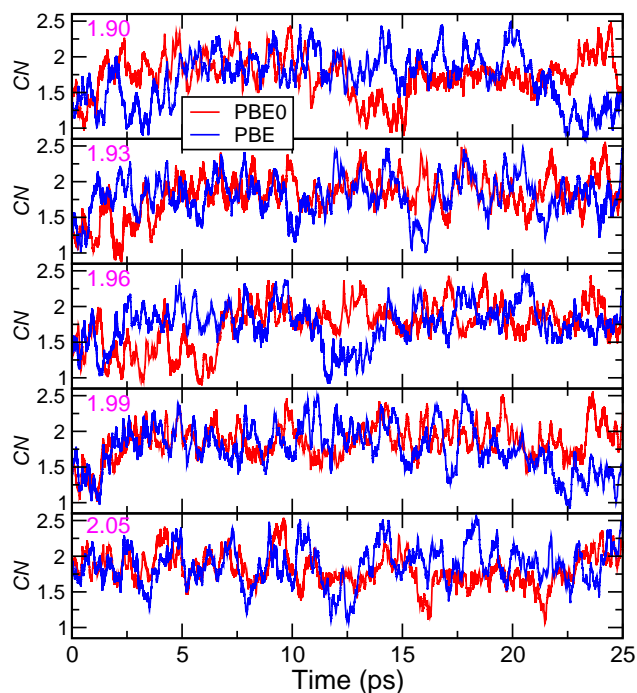


FIG. F.2. Fluctuations in the  $\text{CN}[\text{O}_1 : \text{H}_w]$  CV with simulation time for the umbrella windows near the transition state region (from 1.90 to 2.05 Å) using PBE and PBE0 functionals.

## Appendix G: Convergence of the Free Energy Barriers

### 1. Methyl Formate Hydrolysis

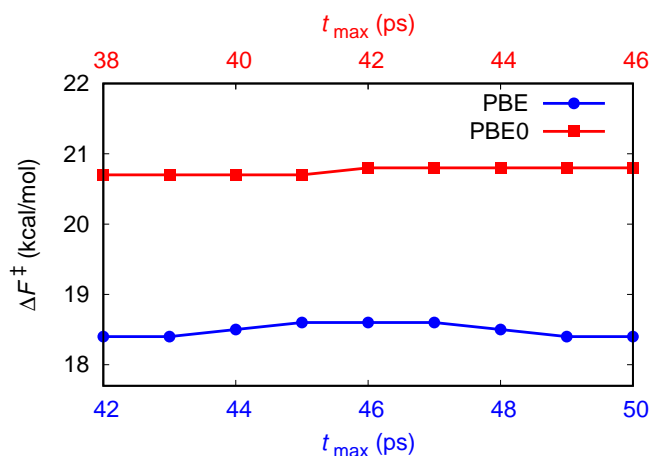


FIG. G.1. Convergence of the free energy barrier ( $\Delta F^\ddagger$ ) for the reaction  $\mathbf{R} \rightarrow \mathbf{P}$  with different  $t_{\max}$  values using PBE and PBE0 density functionals. Here,  $t_{\min} = 20$  ps was taken.

### 2. Protonation State of Active Site Residues of Class-C $\beta$ -Lactamase

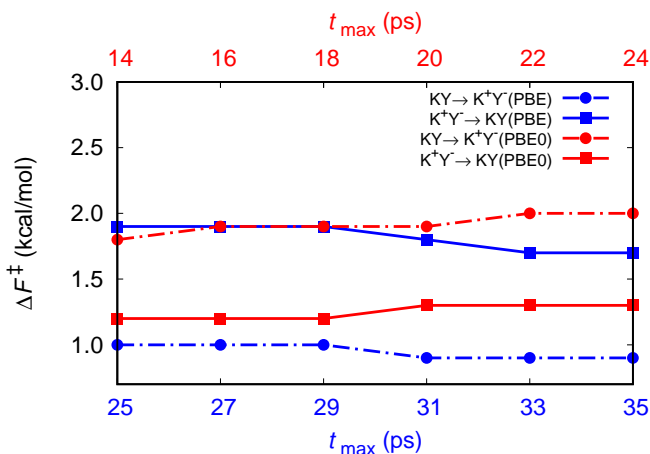


FIG. G.2. Convergence of the free energy barrier ( $\Delta F^\ddagger$ ) with different  $t_{\max}$  values for the reaction  $\mathbf{KY} \rightarrow \mathbf{K}^+\mathbf{Y}^-$  using PBE functional (blue circles) and PBE0 functional (red circles); and  $\mathbf{K}^+\mathbf{Y}^- \rightarrow \mathbf{KY}$  using PBE functional (blue squares) and PBE0 functional (red squares). Here,  $t_{\min} = 15$  ps was taken for PBE functional; and  $t_{\min} = 4$  ps was taken for PBE0 functional.

## REFERENCES

- <sup>1</sup>M. E. Tuckerman, *Statistical Mechanics: Theory and Molecular Simulation* (Oxford University Press, Oxford, 2010).
- <sup>2</sup>A. P. Leach, *Molecular Modelling. Principles and Applications* (Pearson Education Limited, Upper Saddle River, New Jersey, 2001).
- <sup>3</sup>D. Frenkel and B. Smit, *Understanding Molecular Simulation: From Algorithms to Applications* (Academic Press, San Diego, 2002).
- <sup>4</sup>M. E. Tuckerman and G. J. Martyna, "Understanding modern molecular dynamics: Techniques and applications," *J. Phys. Chem. B* **104**, 159–178 (2000).
- <sup>5</sup>D. Marx and J. Hutter, *Ab Initio Molecular Dynamics: Basic Theory and Advanced Methods* (Cambridge University Press, Cambridge, 2009).
- <sup>6</sup>R. Iftimie, P. Minari, and M. E. Tuckerman, "Ab initio molecular dynamics: Concepts, recent developments, and future trends," *Proc. Natl. Acad. Sci. U.S.A.* **102**, 6654–6659 (2005).
- <sup>7</sup>M. E. Tuckerman, "Ab initio molecular dynamics: basic concepts, current trends and novel applications," *J. Phys.: Condens. Matter* **14**, R1297–R1355 (2002).
- <sup>8</sup>M. C. Payne, M. P. Teter, D. C. Allan, T. A. Arias, and J. D. Joannopoulos, "Iterative minimization techniques for ab initio total-energy calculations: molecular dynamics and conjugate gradients," *Rev. Mod. Phys.* **64**, 1045–1097 (1992).
- <sup>9</sup>A. D. Becke, "Density-functional exchange-energy approximation with correct asymptotic behavior," *Phys. Rev. A* **38**, 3098–3100 (1988).
- <sup>10</sup>C. Lee, W. Yang, and R. G. Parr, "Development of the Colle-Salvetti correlation-energy formula into a functional of the electron density," *Phys. Rev. B* **37**, 785–789 (1988).
- <sup>11</sup>J. P. Perdew, K. Burke, and M. Ernzerhof, "Generalized gradient approximation made simple," *Phys. Rev. Lett.* **77**, 3865–3868 (1996).
- <sup>12</sup>W. Koch and M. C. Holthausen, *A Chemist's Guide to Density Functional Theory* (WILEY-VCH, New York, 2001).
- <sup>13</sup>A. J. Cohen, P. Mori-Sánchez, and W. Yang, "Insights into current limitations of density functional theory," *Science* **321**, 792–794 (2008).
- <sup>14</sup>J. P. Perdew and A. Zunger, "Self-interaction correction to density-functional approximations for many-electron systems," *Phys. Rev. B* **23**, 5048–5079 (1981).
- <sup>15</sup>P. Mori-Sánchez, A. J. Cohen, and W. Yang, "Localization and delocalization errors in density functional theory and implications for band-gap prediction," *Phys. Rev. Lett.* **100**, 146401 (2008).
- <sup>16</sup>R. M. Martin, *Electronic Structure: Basic Theory and Practical Methods* (Cambridge University Press, Cambridge, 2004).
- <sup>17</sup>A. D. Becke, "Density-functional thermochemistry. III. The role of exact exchange," *J. Chem. Phys.* **98**, 5648–5652 (1993).
- <sup>18</sup>J. P. Perdew, M. Ernzerhof, and K. Burke, "Rationale for mixing exact exchange with density functional approximations," *J. Chem. Phys.* **105**, 9982–9985 (1996).
- <sup>19</sup>J. Heyd, G. E. Scuseria, and M. Ernzerhof, "Hybrid functionals based on a screened Coulomb potential," *J. Chem. Phys.* **118**, 8207–8215 (2003).
- <sup>20</sup>C. Adamo and V. Barone, "Toward reliable density functional methods without adjustable parameters: The PBE0 model," *J. Chem. Phys.* **110**, 6158–6170 (1999).
- <sup>21</sup>C. J. Cramer and D. G. Truhlar, "Density functional theory for transition metals and transition metal chemistry," *Phys. Chem. Chem. Phys.* **11**, 10757–10816 (2009).
- <sup>22</sup>B. G. Janesko, T. M. Henderson, and G. E. Scuseria, "Screened hybrid density functionals for solid-state chemistry and physics," *Phys. Chem. Chem. Phys.* **11**, 443–454 (2009).
- <sup>23</sup>Q. Wan, L. Spanu, F. Gygi, and G. Galli, "Electronic structure of aqueous sulfuric acid from first-principles simulations with hybrid functionals," *J. Phys. Chem. Lett.* **5**, 2562–2567 (2014).
- <sup>24</sup>A. J. Cohen, P. Mori-Sánchez, and W. Yang, "Challenges for density functional theory," *Chem. Rev.* **112**, 289–320 (2012).
- <sup>25</sup>H. Xiao, J. Tahir-Kheli, and W. A. Goddard III, "Accurate band gaps for semiconductors from density functional theory," *J. Phys. Chem. Lett.* **2**, 212–217 (2011).
- <sup>26</sup>Q. Zhao and H. J. Kulik, "Stable surfaces that bind too tightly: Can range-separated hybrids or DFT+U improve paradoxical descriptions of surface chemistry?" *J. Phys. Chem. Lett.* **10**, 5090–5098 (2019).

- <sup>27</sup>N. Gerrits, E. W. F. Smeets, S. Vuckovic, A. D. Powell, K. Doblhoff-Dier, and G.-J. Kroes, "Density functional theory for molecule-metal surface reactions: When does the generalized gradient approximation get it right, and what to do if it does not," *J. Phys. Chem. Lett.* **11**, 10552–10560 (2020).
- <sup>28</sup>B. G. Janesko and G. E. Scuseria, "Hartree-Fock orbitals significantly improve the reaction barrier heights predicted by semilocal density functionals," *J. Chem. Phys.* **128**, 244112 (2008).
- <sup>29</sup>G. F. Mangiatordi, E. Brémond, and C. Adamo, "DFT and proton transfer reactions: A benchmark study on structure and kinetics," *J. Chem. Theory Comput.* **8**, 3082–3088 (2012).
- <sup>30</sup>T. Todorova, A. P. Seitsonen, J. Hutter, I.-F. W. Kuo, and C. J. Mundy, "Molecular dynamics simulation of liquid water: Hybrid density functionals," *J. Phys. Chem. B* **110**, 3685–3691 (2006).
- <sup>31</sup>C. Zhang, D. Donadio, F. Gygi, and G. Galli, "First principles simulations of the infrared spectrum of liquid water using hybrid density functionals," *J. Chem. Theory Comput.* **7**, 1443–1449 (2011).
- <sup>32</sup>R. A. DiStasio Jr., B. Santra, Z. Li, X. Wu, and R. Car, "The individual and collective effects of exact exchange and dispersion interactions on the ab initio structure of liquid water," *J. Chem. Phys.* **141**, 084502 (2014).
- <sup>33</sup>B. Santra, R. A. DiStasio Jr., F. Martelli, and R. Car, "Local structure analysis in ab initio liquid water," *Mol. Phys.* **113**, 2829–2841 (2015).
- <sup>34</sup>A. Bankura, B. Santra, R. A. DiStasio Jr., C. W. Swartz, M. L. Klein, and X. Wu, "A systematic study of chloride ion solvation in water using van der Waals inclusive hybrid density functional theory," *Mol. Phys.* **113**, 2842–2854 (2015).
- <sup>35</sup>F. Ambrosio, G. Miceli, and A. Pasquarello, "Structural, dynamical, and electronic properties of liquid water: A hybrid functional study," *J. Phys. Chem. B* **120**, 7456–7470 (2016).
- <sup>36</sup>E. Sevgen, F. Giberti, H. Sidky, J. K. Whitmer, G. Galli, F. Gygi, and J. J. de Pablo, "Hierarchical coupling of first-principles molecular dynamics with advanced sampling methods," *J. Chem. Theory Comput.* **14**, 2881–2888 (2018).
- <sup>37</sup>S. Mandal, J. Debnath, B. Meyer, and N. N. Nair, "Enhanced sampling and free energy calculations with hybrid functionals and plane waves for chemical reactions," *J. Chem. Phys.* **149**, 144113 (2018).
- <sup>38</sup>S. Mandal and N. N. Nair, "Efficient computation of free energy surfaces of chemical reactions using ab initio molecular dynamics with hybrid functionals and plane waves," *J. Comput. Chem.* **41**, 1790–1797 (2020).
- <sup>39</sup>S. Chawla and G. A. Voth, "Exact exchange in ab initio molecular dynamics: An efficient plane-wave based algorithm," *J. Chem. Phys.* **108**, 4697–4700 (1998).
- <sup>40</sup>X. Wu, A. Selloni, and R. Car, "Order- $N$  implementation of exact exchange in extended insulating systems," *Phys. Rev. B* **79**, 085102 (2009).
- <sup>41</sup>M. Chen, L. Zheng, B. Santra, H.-Y. Ko, R. A. DiStasio Jr., M. L. Klein, R. Car, and X. Wu, "Hydroxide diffuses slower than hydronium in water because its solvated structure inhibits correlated proton transfer," *Nat. Chem.* **10**, 413–419 (2018).
- <sup>42</sup>F. Gygi, "Compact representations of Kohn-Sham invariant subspaces," *Phys. Rev. Lett.* **102**, 166406 (2009).
- <sup>43</sup>F. Gygi and I. Duchemin, "Efficient computation of Hartree-Fock exchange using recursive subspace bisection," *J. Chem. Theory Comput.* **9**, 582–587 (2013).
- <sup>44</sup>W. Dawson and F. Gygi, "Performance and accuracy of recursive subspace bisection for hybrid DFT calculations in inhomogeneous systems," *J. Chem. Theory Comput.* **11**, 4655–4663 (2015).
- <sup>45</sup>A. P. Gaiduk, C. Zhang, F. Gygi, and G. Galli, "Structural and electronic properties of aqueous NaCl solutions from ab initio molecular dynamics simulations with hybrid density functionals," *Chem. Phys. Lett.* **604**, 89 – 96 (2014).
- <sup>46</sup>A. P. Gaiduk, F. Gygi, and G. Galli, "Density and compressibility of liquid water and ice from first-principles simulations with hybrid functionals," *J. Phys. Chem. Lett.* **6**, 2902–2908 (2015).
- <sup>47</sup>H.-Y. Ko, J. Jia, B. Santra, X. Wu, R. Car, and R. A. DiStasio Jr., "Enabling large-scale condensed-phase hybrid density functional theory based ab initio molecular dynamics. 1. theory, algorithm, and performance," *J. Chem. Theory Comput.* **16**, 3757–3785 (2020).
- <sup>48</sup>H.-Y. Ko, B. Santra, and R. A. DiStasio Jr., "Enabling large-scale condensed-phase hybrid density functional theory based *ab initio* molecular dynamics II: Extensions to the isobaric-isenthalpic and isobaric-isothermal ensembles," (2020), arXiv:2011.07209 [cond-mat.mtrl-sci].
- <sup>49</sup>M. Guidon, F. Schiffmann, J. Hutter, and J. VandeVondele, "Ab initio molecular dynamics using hybrid density functionals," *J. Chem. Phys.* **128**, 214104 (2008).
- <sup>50</sup>E. Liberatore, R. Meli, and U. Rothlisberger, "A versatile multiple time step scheme for efficient ab initio molecular dynamics simulations," *J. Chem. Theory Comput.* **14**, 2834–2842 (2018).
- <sup>51</sup>S. Fatehi and R. P. Steele, "Multiple-time step ab initio molecular dynamics based on two-electron integral screening," *J. Chem. Theory Comput.* **11**, 884–898 (2015).
- <sup>52</sup>M. P. Bircher and U. Rothlisberger, "Exploiting coordinate scaling relations to accelerate exact exchange calculations," *J. Phys. Chem. Lett.* **9**, 3886–3890 (2018).
- <sup>53</sup>M. P. Bircher and U. Rothlisberger, "From a week to less than a day: Speedup and scaling of coordinate-scaled exact exchange calculations in plane waves," *Comput. Phys. Commun.* **247**, 106943 (2020).
- <sup>54</sup>V. Weber, C. Bekas, T. Laino, A. Curioni, A. Bertsch, and S. Fratini, "Shedding light on Lithium/air batteries using millions of threads on the BG/Q supercomputer," in *2014 IEEE 28th International Parallel and Distributed Processing Symposium* (Phoenix, AZ, USA, 2014) pp. 735–744.
- <sup>55</sup>I. Duchemin and F. Gygi, "A scalable and accurate algorithm for the computation of Hartree-Fock exchange," *Comput. Phys. Commun.* **181**, 855 – 860 (2010).
- <sup>56</sup>N. Varini, D. Ceresoli, L. Martin-Samos, I. Girotto, and C. Cavazzoni, "Enhancement of DFT-calculations at petascale: Nuclear magnetic resonance, hybrid density functional theory and Car-Parrinello calculations," *Comput. Phys. Commun.* **184**, 1827–1833 (2013).
- <sup>57</sup>T. A. Barnes, T. Kurth, P. Carrier, N. Wichmann, D. Prendergast, P. R. Kent, and J. Deslippe, "Improved treatment of exact exchange in Quantum ESPRESSO," *Comput. Phys. Commun.* **214**, 52–58 (2017).
- <sup>58</sup>V. Bolnykh, J. M. H. Olsen, S. Meloni, M. P. Bircher, E. Ippoliti, P. Carloni, and U. Rothlisberger, "Extreme scalability of DFT-based QM/MM MD simulations using MiMiC," *J. Chem. Theory Comput.* **15**, 5601–5613 (2019).
- <sup>59</sup>J. Vinson, "Faster exact exchange in periodic systems using single-precision arithmetic," *J. Chem. Phys.* **153**, 204106 (2020).
- <sup>60</sup>S. Mandal and N. N. Nair, "Speeding-up ab initio molecular dynamics with hybrid functionals using adaptively compressed exchange operator based multiple timestepping," *J. Chem. Phys.* **151**, 151102 (2019).
- <sup>61</sup>L. Lin, "Adaptively compressed exchange operator," *J. Chem. Theory Comput.* **12**, 2242–2249 (2016).
- <sup>62</sup>W. Hu, L. Lin, A. S. Banerjee, E. Vecharynski, and C. Yang, "Adaptively compressed exchange operator for large-scale hybrid density functional calculations with applications to the adsorption of water on silicene," *J. Chem. Theory Comput.* **13**, 1188–1198 (2017).
- <sup>63</sup>A. Damle, L. Lin, and L. Ying, "Compressed representation of Kohn-Sham orbitals via selected columns of the density matrix," *J. Chem. Theory Comput.* **11**, 1463–1469 (2015).
- <sup>64</sup>I. Carnimeo, S. Baroni, and P. Giannozzi, "Fast hybrid density-functional computations using plane-wave basis sets," *Electron. Struct.* **1**, 015009 (2019).
- <sup>65</sup>P. Giannozzi, O. Andreussi, T. Brumme, O. Bunau, M. B. Nardelli, M. Calandra, R. Car, C. Cavazzoni, D. Ceresoli, M. Cococcioni, N. Colonna, I. Carnimeo, A. D. Corso, S. de Gironcoli, P. Delugas, R. A. DiStasio Jr., A. Ferretti, A. Floris, G. Fratesi, G. Fugallo, R. Gebauer, U. Gerstmann, F. Giustino, T. Gorni, J. Jia, M. Kawamura, H.-Y. Ko, A. Kokalj, E. Küçükbenli, M. Lazzeri, M. Marsili, N. Marzari, F. Mauri, N. L. Nguyen, H.-V. Nguyen, A. Otero-de-la Roza, L. Paulatto, S. Poncé, D. Rocca, R. Sabatini, B. Santra, M. Schlipf, A. P. Seitsonen, A. Smogunov, I. Timrov, T. Thonhauser, P. Umari, N. Vast, X. Wu, and S. Baroni, "Advanced ca-

- pabilities for materials modelling with Quantum ESPRESSO,” *J. Phys.: Condens. Matter* **29**, 465901 (2017).
- <sup>66</sup>M. Tuckerman, B. J. Berne, and G. J. Martyna, “Reversible multiple time scale molecular dynamics,” *J. Chem. Phys.* **97**, 1990–2001 (1992).
- <sup>67</sup>J. Hutter et al., *CPMD: An Ab Initio Electronic Structure and Molecular Dynamics Program*, see <http://www.cpmd.org> (accessed on December 31, 2020).
- <sup>68</sup>T. Klöffel, G. Mathias, and B. Meyer, “Integrating state of the art compute, communication, and autotuning strategies to multiply the performance of ab initio molecular dynamics on massively parallel multi-core supercomputers,” *Comput. Phys. Commun.* **260**, 107745 (2021).
- <sup>69</sup>N. Troullier and J. L. Martins, “Efficient pseudopotentials for plane-wave calculations,” *Phys. Rev. B* **43**, 1993–2006 (1991).
- <sup>70</sup>G. J. Martyna, M. L. Klein, and M. Tuckerman, “Nosé–Hoover chains: The canonical ensemble via continuous dynamics,” *J. Chem. Phys.* **97**, 2635–2643 (1992).
- <sup>71</sup>J. Kolafa, “Time-reversible always stable predictor–corrector method for molecular dynamics of polarizable molecules,” *J. Comput. Chem.* **25**, 335–342 (2004).
- <sup>72</sup>S. Awasthi, V. Kapil, and N. N. Nair, “Sampling free energy surfaces as slices by combining umbrella sampling and metadynamics,” *J. Comput. Chem.* **37**, 1413–1424 (2016).
- <sup>73</sup>G. M. Torrie and J. P. Valleau, “Monte Carlo free energy estimates using non-Boltzmann sampling: Application to the sub-critical Lennard-Jones fluid,” *Chem. Phys. Lett.* **28**, 578–581 (1974).
- <sup>74</sup>A. Barducci, G. Bussi, and M. Parrinello, “Well-tempered metadynamics: A smoothly converging and tunable free-energy method,” *Phys. Rev. Lett.* **100**, 020603 (2008).
- <sup>75</sup>S. Kumar, J. M. Rosenberg, D. Bouzida, R. H. Swendsen, and P. A. Kollman, “The weighted histogram analysis method for free-energy calculations on biomolecules. I. The method,” *J. Comput. Chem.* **13**, 1011–1021 (1992).
- <sup>76</sup>R. Tripathi and N. N. Nair, “Thermodynamic and kinetic stabilities of active site protonation states of class-c  $\beta$ -lactamase,” *J. Phys. Chem. B* **116**, 4741–4753 (2012).
- <sup>77</sup>T. E. Cheatham III, P. Cieplak, and P. A. Kollman, “A modified version of the Cornell et al. force field with improved sugar pucker phases and helical repeat,” *J. Biomol. Struct. Dyn.* **16**, 845–862 (1999).
- <sup>78</sup>A. Laio, J. VandeVondele, and U. Rothlisberger, “A Hamiltonian electrostatic coupling scheme for hybrid Car-Parrinello molecular dynamics simulations,” *J. Chem. Phys.* **116**, 6941–6947 (2002).
- <sup>79</sup>*Intel Xeon CPU E5-2670v2 (20 cores/node) with 128 GB of RAM per node.*
- <sup>80</sup>J. P. Guthrie, “Hydration of carboxylic acids and esters. evaluation of the free energy change for addition of water to acetic and formic acids and their methyl esters,” *J. Am. Chem. Soc.* **95**, 6999–7003 (1973).
- <sup>81</sup>J. F. Marlier, T. G. Frey, J. A. Mallory, and W. W. Cleland, “Multiple isotope effect study of the acid-catalyzed hydrolysis of methyl formate,” *J. Org. Chem.* **70**, 1737–1744 (2005).
- <sup>82</sup>O. Jogunola, T. Salmi, K. Eränen, J. Wärnå, M. Kangas, and J.-P. Mikkola, “Reversible autocatalytic hydrolysis of alkyl formate: Kinetic and reactor modeling,” *Ind. Eng. Chem. Res.* **49**, 4099–4106 (2010).
- <sup>83</sup>T. D. Vu, A. Seidel-Morgenstern, S. Grüner, and A. Kienle, “Analysis of ester hydrolysis reactions in a chromatographic reactor using equilibrium theory and a rate model,” *Ind. Eng. Chem. Res.* **44**, 9565–9574 (2005).
- <sup>84</sup>J. P. Guthrie, “Hydration of thioesters. evaluation of the free-energy changes for the addition of water to some thioesters, rate-equilibrium correlations over very wide ranges in equilibrium constants, and a new mechanistic criterion,” *J. Am. Chem. Soc.* **100**, 5892–5904 (1978).
- <sup>85</sup>C.-G. Zhan, D. W. Landry, and R. L. Ornstein, “Reaction pathways and energy barriers for alkaline hydrolysis of carboxylic acid esters in water studied by a hybrid supermolecule-polarizable continuum approach,” *J. Am. Chem. Soc.* **122**, 2621–2627 (2000).
- <sup>86</sup>J. R. Pliego, Jr. and J. M. Riveros, “A theoretical analysis of the free-energy profile of the different pathways in the alkaline hydrolysis of methyl formate in aqueous solution,” *Chem. Eur. J.* **8**, 1945–1953 (2002).
- <sup>87</sup>J. Pranata, “Ab initio study of the base-catalyzed hydrolysis of methyl formate,” *J. Phys. Chem.* **98**, 1180–1184 (1994).
- <sup>88</sup>H. Gunaydin and K. N. Houk, “Molecular dynamics prediction of the mechanism of ester hydrolysis in water,” *J. Am. Chem. Soc.* **130**, 15232–15233 (2008).
- <sup>89</sup>S. Tolosa Arroyo, A. Hidalgo García, M. Moreno Alvero, and J. A. Sansón Martín, “Theoretical study of the neutral hydrolysis of methyl formate via a concerted and stepwise water-assisted mechanism using free-energy curves and molecular dynamics simulation,” *Struct. Chem.* **22**, 909–915 (2011).
- <sup>90</sup>B. P. Callahan, Y. Yuan, and R. Wolfenden, “The burden borne by urease,” *J. Am. Chem. Soc.* **127**, 10828–10829 (2005).
- <sup>91</sup>A. L. L. East, “On the hydrolysis mechanisms of amides and peptides,” *Int. J. Chem. Kinet.* **50**, 705–709 (2018).
- <sup>92</sup>E. Y. Klein, T. P. Van Boeckel, E. M. Martinez, S. Pant, S. Gandra, S. A. Levin, H. Goossens, and R. Laxminarayan, “Global increase and geographic convergence in antibiotic consumption between 2000 and 2015,” *Proc. Nat. Acad. Sci.* **115**, E3463–E3470 (2018).
- <sup>93</sup>C. L. Tooke, P. Hinchliffe, E. C. Bragginton, C. K. Colenso, V. H. Hirvonen, Y. Takebayashi, and J. Spencer, “ $\beta$ -lactamases and  $\beta$ -lactamase inhibitors in the 21st century,” *J. Mol. Biol.* **431**, 3472–3500 (2019).
- <sup>94</sup>K. Bush, “Bench-to-bedside review: The role of  $\beta$ -lactamases in antibiotic-resistant Gram-negative infections,” *Crit. Care* **14**, 224 (2010).
- <sup>95</sup>C. Bebrone, P. Lassaux, L. Vercheval, J.-S. Sohler, A. Jehaes, E. Sauvage, and M. Galleni, “Current challenges in antimicrobial chemotherapy,” *Drugs* **70**, 651–679 (2010).
- <sup>96</sup>R. Tripathi and N. N. Nair, “Deacylation mechanism and kinetics of acyl-enzyme complex of class-c  $\beta$ -lactamase and cephalothin,” *J. Phys. Chem. B* **120**, 2681–2690 (2016).
- <sup>97</sup>R. Tripathi and N. N. Nair, “Mechanism of acyl-enzyme complex formation from the Henry–Michaelis complex of class-c  $\beta$ -lactamases with  $\beta$ -lactam antibiotics,” *J. Am. Chem. Soc.* **135**, 14679–14690 (2013).
- <sup>98</sup>S. Awasthi, S. Gupta, R. Tripathi, and N. N. Nair, “Mechanism and kinetics of aztreonam hydrolysis catalyzed by class-c  $\beta$ -lactamase: A temperature-accelerated sliced sampling study,” *J. Phys. Chem. B* **122**, 4299–4308 (2018).
- <sup>99</sup>C. K. Das and N. N. Nair, “Elucidating the molecular basis of avibactam mediated inhibition of class a  $\beta$ -lactamases,” *Chem. Eur. J.* **26**, 9639–9651 (2020).
- <sup>100</sup>C. K. Das and N. N. Nair, “Hydrolysis of cephalexin and meropenem by New Delhi metallo- $\beta$ -lactamase: the substrate protonation mechanism is drug dependent,” *Phys. Chem. Chem. Phys.* **19**, 13111–13121 (2017).
- <sup>101</sup>F. Zhu and G. Hummer, “Convergence and error estimation in free energy calculations using the weighted histogram analysis method,” *J. Comput. Chem.* **33**, 453–465 (2012).